*J. Fluid Mech.* (1982), *vol.* 118, *pp.* 341–377
*Printed in Great Britain*



# Numerical investigation of turbulent channel flow

By PARVIZ MOIN AND JOHN KIM
Department of Mechanical Engineering, Stanford University, Stanford, California 94305, U.S.A.

(Received 3 August 1981)

Fully developed turbulent channel flow has been simulated numerically at Reynolds number 13800, based on centre-line velocity and channel half-width. The large-scale flow field has been obtained by directly integrating the filtered, three-dimensional, time-dependent Navier–Stokes equations. The small-scale field motions were simulated through an eddy-viscosity model. The calculations were carried out on the ILLIAC IV computer with up to 516096 grid points.

The computed flow field was used to study the statistical properties of the flow as well as its time-dependent features. The agreement of the computed mean-velocity profile, turbulence statistics, and detailed flow structures with experimental data is good. The resolvable portion of the statistical correlations appearing in the Reynolds-stress equations are calculated. Particular attention is given to the examination of the flow structure in the vicinity of the wall.

## 1. Introduction

Large-eddy simulation (LES) is a relatively new approach to the calculation of turbulent flows. The basic idea stems from two experimental observations. First, the large-scale structure of turbulent flows varies greatly from flow to flow (e.g. jets *vs.* boundary layers) and is consequently difficult, if not impossible, to model in a general way. Secondly, the small-scale turbulence structures are nearly isotropic, very universal in character (Chapman 1979), and hence much more amenable to general modelling. In LES, one actually calculates the large-scale motions in a time-dependent, three-dimensional computation, using for the large-scale field dynamical equations that incorporate simple models for small-scale turbulence. Only the part of the turbulence field with scales that are small relative to overall dimensions of the flow field is modelled. This is in contrast to phenomenological turbulence modelling, in which all the deviations from the mean velocity profile are modelled.

A typical LES calculation for wall-bounded turbulent flows imposes a great demand on computer speed and memory. At present, therefore, the use of LES for practical engineering applications is admittedly uneconomical. However, for simple flows, such calculations are just within reach of the largest present computers. The information generated by these computations can in turn be used as a powerful research tool in studies of the structure and dynamics of turbulence. In addition, the various correlations that can be obtained from the computed large-scale field may be used in developing phenomenological turbulence models for complex flows. These are the considerations that motivate the present development of the LES method.

The first application of LES was made by Deardorff (1970), who simulated a turbulent channel flow at an indefinitely large Reynolds number. In this pioneering work he

showed that three-dimensional computation of turbulence (at least for simple flows) is feasible. Using only 6720 grid points, he was able to predict several features of turbulent channel flow with a fair amount of success. Of particular significance was the demonstration of the potential of LES for use in basic studies of turbulence.

Following Deardorff's work, Schumann (1973, 1975) also calculated turbulent channel flow and extended the method to cylindrical geometries (annuli). He used up to ten times more grid points (65536) than Deardorff, and an improved subgrid scale (SGS) model. In addition to dividing SGS stresses into a locally isotropic part and an inhomogeneous part, he employed a separate partial differential equation for SGS turbulent kinetic energy. However, the added differential equation did not improve the results over the calculations in which only an eddy viscosity model was used (Schumann 1975).

Grötzbach & Schumann (1979) extended their channel-flow calculations to account for temperature fluctuations and heat transfer. Later extensions by Grötzbach include calculations of secondary flows in partly roughened channels, inclusion of buoyancy effects, and liquid metal flows in plane channels and annuli. A recent review of this group's work in LES was given by Schumann, Grötzbach & Kleiser (1980).

In all of the above computations, the dynamics of the inner region of the boundary layer (viscous sublayer and buffer layer) was essentially ignored. It is in this region that virtually all of the production of turbulence kinetic energy takes place (Townsend 1956; Kim, Kline & Reynolds 1971). Artificial boundary conditions in the logarithmic region were used to simulate the inner layers. Aside from the fact that these boundary conditions are designed to be consistent in the mean with the law of the wall, there is little justification or experimental evidence to warrant their use for the detailed flow field. However, the computations of Deardorff (1970) and especially those of the Karlsruhe group have produced successful comparisons with experimental data in the regions away from the walls. With a relatively modest number of grid points, they have been able to extract considerable information of practical interest from their computations.

The first numerical simulation of turbulent channel flow that computed rather than modelled the flow in the immediate neighbourhood of the wall was that of Moin, Reynolds & Ferziger (1978). In this calculation only 16 uniformly spaced grid points were used in each of the streamwise ($x$) and spanwise ($z$) directions, and 65 non-uniformly spaced grid points in the direction normal to the walls. The computational grid resolution in the lateral directions was inadequate for resolving the experimentally observed coherent structures in the viscous sublayer. Nevertheless, the computations did display some of the well-established features of the flow in the wall region. The results of this computation were encouraging enough to justify the undertaking of the present calculations.

In this paper, we describe our numerical studies of incompressible turbulent channel flow with up to 516096 grid points. Particular attention is given to the investigation of the detailed flow structures. The Reynolds number $Re_\tau$ based on shear velocity $u_\tau$ and channel half-width was set at 640. The corresponding Reynolds number based on centre-line velocity and channel half-width is about 13800 (Hussain & Reynolds 1975). The results of this work can be summarized briefly by stating that, in the present computations, the calculated mean-velocity profile and turbulence statistics are in good agreement with the experimental data. The detailed time-dependent flow

structures are strikingly similar to those observed experimentally. In addition, the resolvable portion of several statistical correlations that play an important role in phenomenological turbulence modelling are computed. These results tend to indicate that the LES method can be used very effectively in supplementing laboratory measurements of turbulent shear flows.

## 2. Governing equations for the large-scale field

In LES, each flow variable $f$ is decomposed as follows:

$$f = \bar{f} + f', \tag{2.1}$$

where $\bar{f}$ is the large-scale component and $f'$ is the residual field. Following Leonard (1974), we define the large-scale field as

$$\bar{f}(x_1, x_2, x_3) = \int_D \prod_{i=1}^{3} G_i(x_i, x_i')\, f(x_1', x_2', x_3')\, dx_1'\, dx_2'\, dx_3', \tag{2.2}$$

where $G_i$ is the filter function in the $i$-direction and the integral is extended over the whole flow field. In planes parallel to the walls in which the flow is statistically homogeneous, we use the Gaussian filter function

$$G_i(x_i, x_i') = \left(\frac{6}{\pi\Delta_i}\right)^{\frac{1}{2}} \exp\left[-6(x_i - x_i')^2/\Delta_i^2\right] \quad (i = 1, 3). \tag{2.3}$$

Here, $\Delta_i = 2h_i$ (Kwak, Reynolds & Ferziger 1975), $h_i$ is the computational mesh size in the $i$-direction, and subscripts 1 and 3 refer respectively to the streamwise and spanwise directions. The corresponding integrals in (2.2) are extended over the entire $(x_1, x_3)$-plane. The width of the Gaussian function characterizes the size of the smallest eddies in the homogeneous directions that are retained in the filtered field (the largest eddies in the residual field).

Owing to variation of turbulence length scale in the direction normal to the walls, $x_2$, one should use a filter with a variable width, $\Delta_2(x_2)$. In this direction a sectionally continuous 'top-hat' filter function was used. Let $x_{2,j}$ be the location of the $j$th computational grid point in the vertical direction; we define the filter function $G_2$ for the control volume surrounding $x_{2,j}$ as follows:

$$G_2(x_2, x_2') = \begin{cases} (\Delta^+(x_2) + \Delta^-(x_2))^{-1} & \text{for} \quad x_2 - \Delta^-(x_2) < x_2' < x_2 + \Delta^+(x_2), \\ 0 & \text{for} \quad x_2' > x_2 + \Delta^+(x_2), \quad x_2' < x_2 - \Delta^-(x_2), \end{cases} \tag{2.4}$$

where

$$\left.\begin{aligned} \Delta^+(x_2) &= \tfrac{1}{2}(x_{2,j+1} - x_{2,j}) \\ \Delta^-(x_2) &= \tfrac{1}{2}(x_{2,j} - x_{2,j-1}) \end{aligned}\right\} \quad \text{for} \quad \tfrac{1}{2}(x_{2,j} + x_{2,j-1}) < x_2 < \tfrac{1}{2}(x_{2,j+1} + x_{2,j}).$$

The functions $\Delta^+$ and $\Delta^-$ are sectionally constant functions of $x_2$; therefore, in the open neighbourhood surrounding each computational grid point, $x_{2,j} - \Delta^- < x_2 < x_{2,j} + \Delta^+$, $d\Delta^+/dx_2 = d\Delta^-/dx_2 = 0$. An important consequence of this property of $\Delta^+$ and $\Delta^-$ and the form of $G_1$ and $G_3$ (functions of $x_i - x_i'$, $i = 1, 3$) is the commutivity of the filtering operation and partial-differentiation operators in these neighbourhoods and in particular at the computational grid points (see Moin *et al.* 1978), i.e.

$$\overline{\frac{\partial f}{\partial x_2}} = \frac{\partial \bar{f}}{\partial x_2}. \tag{2.5}$$

Note that, with the application of $G_2$, the filtered variable $\bar{f}$ will be sectionally continuous, and the filtering in (2.3) is interpreted as an average over grid spacings in the $x_2$ direction. This is a step prior to complete discretization of flow variables for numerical computation (§3).

Schumann (1975) and coworkers use a filtering function similar to (2.4) in all spatial directions. When applying this averaging process to the Navier–Stokes equations, they evaluate the integral in the direction of the derivatives analytically, and then have to deal with averages over the faces of the control volumes. This process introduces three types of surface-averaged as well as volume-averaged variables. The extra variables have to be related to each other in some way.

Now, applying the filtering operation (2.2) to the incompressible Navier–Stokes and continuity equations, we obtain the dynamical equations of the large-scale flow field,

$$\frac{\partial \bar{u}_i}{\partial t} - \epsilon_{ijk}\overline{\bar{u}_j \bar{\omega}_k} + \frac{\partial}{\partial x_i}\tfrac{1}{2}\overline{\bar{u}_j \bar{u}_j} = -\frac{\partial P}{\partial x_i} + \delta_{i1} - \frac{\partial}{\partial x_j}\tau_{ij} + \frac{1}{Re_\tau}\frac{\partial^2 \bar{u}_i}{\partial x_j \partial x_j}, \tag{2.6}$$

$$\frac{\partial \bar{u}_i}{\partial x_i} = 0, \tag{2.7}$$

where we have decomposed $u_i$ as in (2.1) and

$$\omega_k = \epsilon_{pqk}\frac{\partial \bar{u}_q}{\partial x_p}, \quad \tau_{ij} = Q_{ij} - \tfrac{1}{3}Q_{kk}\delta_{ij}, \tag{2.8a}$$

$$Q_{ij} = \overline{u_i' u_j'} + \overline{u_j' \bar{u}_i} + \overline{\bar{u}_j u_i'}, \quad P = \frac{\bar{p}}{\rho} + \tfrac{1}{3}Q_{kk}. \tag{2.8b}$$

Here, the variables are non-dimensionalized using the channel half-width $\delta$ and the wall shear velocity $u_\tau$. The calculations were carried out for a fixed streamwise mean-pressure gradient which is accounted for by the $\delta_{i1}$ term in the momentum equation (2.6).

There are two points associated with (2.6) that require further explanation. First, the convective term $\partial(u_i u_j)/\partial x_j$, is written in the equivalent but more cumbersome form

$$-\epsilon_{ijk} u_j \omega_k + \frac{\partial}{\partial x_i}(\tfrac{1}{2}u_j u_j).$$

This was done because it can be shown (Mansour *et al.* 1979) that, in the absence of time-differencing errors, with this form conservation of energy, momentum, and circulation in inviscid flows will be obtained when virtually any difference scheme is applied to (2.6). Secondly, it should be noted that the so-called Leonard (1974) stress term

$$\lambda_{ij} = \overline{\bar{u}_i \bar{u}_j} - \bar{u}_i \bar{u}_j \tag{2.9}$$

is *not* equal to zero. One has the option of calculating the term with double bars explicitly, or, as Deardorff (1970) has done, to incorporate $\lambda_{ij}$ in whatever modelling assumption is used for $\tau_{ij}$ (see §3). In the present work, with respect to the Gaussian filter in the horizontal directions where the partial derivatives are calculated pseudospectrally (§5), we have chosen the former option. In §6 we shall show that $\lambda_{ij}$ can be quite significant; hence including it with $\tau_{ij}$ is not recommended. With respect to the top-hat filter in the $x_2$ direction where the derivatives are evaluated by second-order finite-difference schemes, the latter option was chosen. Here it can be shown that (Shaanan,

Ferziger & Reynolds 1975) $\lambda_{ij}$ is of the same form and order as the truncation error of the finite-difference scheme; hence its explicit calculation is not justified. However, when higher-order finite-difference schemes or spectral methods are used to evaluate the derivatives in the $x_2$ direction, $\lambda_{ij}$ should be calculated explicitly. It should be pointed out that, when higher-order finite-difference schemes are used in conjunction with staggered grids (Antonopoulos-Domis 1981), the required averaging of the variables across the grid cells will account partially for $\lambda_{ij}$.

## 3. Residual-stress model

The basic idea behind the large-eddy simulation is that the large-scale motions, which are calculated explicitly, provide most of the important turbulent transport, and hence the influence of the small eddies can be modelled relatively crudely. In the present calculations, we have used an eddy viscosity model for $\tau_{ij}$ similar to that used by Schumann (1975):

$$\tau_{ij} = -2\nu_{\mathrm{T}}(S_{ij} - \langle S_{ij}\rangle) - 2\nu_{\mathrm{T}}^{*}\langle S_{ij}\rangle, \tag{3.1}$$

where

$$S_{ij} = \frac{1}{2}\left(\frac{\partial \bar{u}_i}{\partial x_j} + \frac{\partial \bar{u}_j}{\partial x_i}\right),$$

and $\langle\ \rangle$ denotes the average over a plane parallel to the walls. The small-scale eddy viscosities $\nu_{\mathrm{T}}$ and $\nu_{\mathrm{T}}^{*}$ represent the action of the unresolved scales of motion on those that are resolved. Hence, as the resolution gets better, $\nu_{\mathrm{T}}$ and $\nu_{\mathrm{T}}^{*}$ should get smaller. Since the filter widths represent the largest length scales that are *not* resolved, these widths are the characteristic size of the largest (and hence most important) residual motions. The first term in (3.1) with

$$\nu_{\mathrm{T}} = (C_{\mathrm{s}}\Delta)^2\,[2(S_{ij} - \langle S_{ij}\rangle)\,(S_{ij} - \langle S_{ij}\rangle)]^{\frac{1}{2}} \tag{3.2}$$

is Smagorinsky's model, and can be derived from equating the subgrid scale (SGS) production and dissipation in homogeneous turbulence. This model was used successfully in the numerical simulation of the decay of isotropic turbulence by Mansour *et al.* (1979) and by Deardorff (1970) (with $S_{ij} - \langle S_{ij}\rangle$ replaced by $S_{ij}$) in the calculation of the core region of turbulent channel flow. In the expression (3.2) for $\nu_{\mathrm{T}}$, $\Delta$ is the characteristic length scale of the largest subgrid-scale eddies, here assumed to be (Deardorff 1970)

$$\Delta = (\Delta_1\Delta_2\Delta_3)^{\frac{1}{3}}. \tag{3.3}$$

$C_{\mathrm{s}}$ is a dimensionless constant, and $\Delta_i$ is the filter width in the $i$-direction. In addition, in order to account for low-Reynolds-number SGS turbulence near the wall, the above expression for $\Delta$ was multiplied by the Van Driest (1956) exponential damping function $1-\exp(-y^+/A^+)$, with $A^+ = 25$ and $y^+ = y_{\mathrm{w}}u_\tau/\nu$, the distance to the nearest wall in the wall units. In all the calculations reported here, which were performed with different grid sizes, the value of $C_{\mathrm{s}} = 0{\cdot}065$ was used. Numerical experiments indicated that the use of a value much larger than this resulted in excessive damping of the resolvable turbulence. When lower values of $C_{\mathrm{s}}$ were used, excess energy accumulated near the high-wavenumber end of one-dimensional energy spectra. In general, however, the computed turbulence intensities were rather insensitive to small perturbations ($\simeq 20\,\%$) of $C_{\mathrm{s}}$. Note that the above value of $C_{\mathrm{s}}$ corresponds to $C_{\mathrm{s}} = 0{\cdot}1$, used by Deardorff (1970), if $\Delta_i$ in (3.3) is replaced by $h_i$.

Near the wall the important large-scale structures are the 'streaks' (Kline *et al.* 1967). These structures are relatively finely spaced in the spanwise direction. Their mean spacing characterizes the length scale of the eddies in the viscous sublayer (and hence the thickness of the viscous sublayer). Thus in a calculation with inadequate resolution in the spanwise direction, the thickness of the viscous sublayer will probably be larger than its physical counterpart. This in turn will lead to lower gradients of the computed mean velocity profile, and consequently insufficient production of the resolvable turbulent kinetic energy. Therefore, in order to account for the effect of some of the streaks that reside in SGS motion on the mean-velocity profile, the second term in (3.1) was introduced in the model for $\tau_{ij}$. As was mentioned earlier, Schumann (1975) has also decomposed SGS stresses into two parts, as in (3.1). The first was to account for locally isotropic SGS stresses, and the second to account for inhomogeneities due to the nonzero component of mean strain.

In the present study, the eddy viscosity $\nu_{\mathrm{T}}^*$ is defined as follows:

$$\nu_{\mathrm{T}}^* = c(D\Delta_3)^2 (2\langle S_{ij}\rangle \langle S_{ij}\rangle)^{\frac{1}{2}}, \tag{3.4}$$

where $c = 0{\cdot}065$ is a dimensionless constant and $D = 1-\exp(-y^{+2}/A^{+2})$ is a wall-damping function with $A^+ = 25$, as before. It should be pointed out that the characteristic length scale associated with $\nu_{\mathrm{T}}^*$ is $\Delta_3$, the filter width in the spanwise direction. As the resolution in the $z$-direction is improved, $\nu_{\mathrm{T}}^*$ will approach zero. Moreover, it should be noted that, owing to its functional form (function of $y$ only), $\nu_{\mathrm{T}}^*$ does not appear directly in the governing equations for the resolvable portions of turbulence stresses, and hence does not contribute to the dissipation terms in these equations. This is in contrast to $\nu_{\mathrm{T}}$, which will supplement the molecular viscosity as a dissipating agent for the resolvable turbulence stresses. However, $\nu_{\mathrm{T}}^*$ contributes to the dissipation of mean kinetic energy $\frac{1}{2}\langle\bar{u}\rangle^2$, and therefore indirectly to the production of resolvable turbulence stresses. The value of $c$ in (3.4) was chosen to be $0{\cdot}065$ from numerical experiment. It is approximately the minimum value with which the resolvable turbulent kinetic energy can be maintained (i.e. it did not decay indefinitely). This numerical experiment was performed with one of the computations reported in table 1 (case 1), but the same constant was used in all the other calculations reported here.

## 4. The computational grid

Three factors influence the choice of the computational grid. First, the mesh size should be small enough to resolve the important scales of motion in the flow. Secondly, the computational domain should be large enough that artificialities of the boundary conditions do not influence the statistics of the solution in an undesirable way. Thirdly, the availability of computer resources restricts the size of calculation that can be done.

In the direction normal to the walls ($-1 \leqslant y \leqslant 1$)† 63 grid points with non-uniform spacings were distributed. The following transformation gives the location of grid points in this direction:

$$y_j = \tfrac{1}{2}\tanh[\xi_j \operatorname{artanh} a], \tag{4.1}$$

where

$$\xi_j = -1+2(j-1)/(N_2-1) \quad (j = 1, 2, \ldots, N_2).$$

† For notational simplicity, we occasionally shift from $(x_1, x_2, x_3)$, $(u_1, u_2, u_3)$ to $(x, y, z)$, $(u, v, w)$.

| Case | $N_1$ | $N_3$ | $L_1/\delta$ | $L_3/\delta$ | $h_1^+$ | $h_3^+$ | $h_1/\delta$ | $h_3/\delta$ | Integration time† | Average time† |
|---|---|---|---|---|---|---|---|---|---|---|
| 1 | 64 | 64 | $4\pi$ | $\frac{2}{3}\pi$ | 125·7 | 20·9 | 0·196 | 0·033 | 4·0 | 1·6 |
| 2 | 64 | 128 | $4\pi$ | $\pi$ | 125·7 | 15·7 | 0·196 | 0·025 | 3·65 | 0·75 |
| 3 | 64 | 128 | $3\pi$ | $\pi$ | 94·2 | 15·7 | 0·147 | 0·025 | 3·9 | 1·6 |
| 4 | 64 | 128 | $2\pi$ | $\pi$ | 62·8 | 15·7 | 0·098 | 0·025 | 4·6 | 2·3 |

† In $\delta/u_\tau$ units

TABLE 1. Specifications of the computed cases

Here $N_2$ is the total number of grid points in the $y$-direction, and $a$ is the adjustable parameter of the transformation ($0 < a < 1$); a large value of $a$ distributes more points near the walls. In our computations we have used $a = 0{\cdot}98346$, $N_2 = 63$. This value of $a$ was selected so that the above grid distribution in the $y$-direction is sufficient to resolve the viscous sublayer ($y^+ < 5$).

The selection of the length of the computational box in the streamwise and spanwise directions is *initially* guided by the two-point correlation measurements of Comte-Bellot (1963). Her data show that the correlation between velocity fluctuations at two points away from the walls‡ separated in $x_1$ becomes negligible at an $x_1$ separation of $3{\cdot}2\delta$. The correlation between motions at two points (away from the walls) separated in $x_3$ becomes negligible beyond an $x_3$ separation of $1{\cdot}6\delta$. Thus, if we wish to employ periodic boundary conditions in the $x_1$ and $x_3$ directions, we must choose a computational domain approximately twice as large as these dimensions. This is to prevent these simple but artificial boundary conditions from seriously influencing the results (Schumann 1973). It should be noted, however, that the *computed* two-point correlation functions provide sufficient information regarding the adequacy of the computational domain. If, for example, in the $x_1$ direction the length $L_1$ of the computational box is too short, the computed profile(s) of $R_{ii}(y, r)$ does not decay sufficiently in the neighbourhood of $r = \frac{1}{2}L_1$, and hence $L_1$ should be increased.

In the wall region, the important large-scale structures are the 'streaks' (Kline *et al.* 1967). These have a mean spanwise spacing corresponding to $\lambda_{3m}^+ \simeq 100$, with the most probable spanwise spacing $\lambda_{3p}^+$, about 80 in the wall units. In addition, Kline *et al.* (1967) and Clark & Markland (1970) occasionally observed U-shaped vortices in the inner region. In the studies of Clark & Markland, the average streamwise spacing of these structures was found to be $\lambda_{1m}^+ = 440$. For the present computation at $Re_\tau \simeq 640$, these correspond to dimensionless spacings of

$$\lambda_{1m} = 440/640 = 0{\cdot}687, \quad \lambda_{3p} = 80/640 = 0{\cdot}125.$$

Table 1 shows the characteristics of the computational grid networks in four different calculations reported here. In this table, $N_i$ is the number of grid points; $L_i$ is the length of the computational box; $h_i$ is the grid spacing in the $i$-direction, and subscripts 1 and 3 refer respectively to the streamwise and spanwise directions. The $L_1/\delta$ and $L_3/\delta$ entries in table 1 show that, except for case 1, where $L_3 < 3{\cdot}2\delta$,§ the size of the computational domain in all other cases appears to be large enough to accommodate the important

‡ Data are not available near the wall.

§ In this case, the computed two-point correlation functions $R_{33}(y, r_3)$ (for $y > 0{\cdot}2\delta$) indicate that $L_3$ is not sufficiently long.

large eddies. Furthermore, since the pseudospectral method (§ 5) is used to approximate the derivatives in the streamwise and spanwise directions, the computational grid resolution (at least for cases 2, 3 and 4) appears to be just adequate to resolve structures with $\lambda_{1m}$ and $\lambda_{3p}$ spacing in the $x_1$ and $x_3$ directions, respectively. It is emphasized that the above values for $\lambda_{1m}$ and $\lambda_{3p}$ are based on an ensemble of measurements, and, at a given instant, structures with a finer spacing than $\lambda_{3p}$ and $\lambda_{1m}$ can be formed which cannot be resolved with the current grid resolution. Thus, we cannot expect the present calculations to reveal the streaky structures in the viscous sublayer with *mean* spacing equal to $\lambda_{3m}$. As we shall see, however, calculations do produce streaks at the finest scale permitted by the grid.

Finally, we mention that the grid meshes for pressure do not coincide with grid meshes for velocities. Grid points for $P$ are located midway between those for $\bar{u}_i$. The equation of continuity is enforced at node points for $P$, whereas the momentum equations are evaluated at node points for $\bar{u}_i$. Note that, in contrast to the conventional staggered grid system (Harlow & Welch 1965), in which the three velocity components are defined at different node points, in the present grid system all the velocities are defined at the same grid points. This will allow for convenient application of the wall-boundary conditions.

## 5. The numerical method

Partial derivatives in the $x_1$ and $x_3$ directions were evaluated pseudospectrally (Orszag 1972). This involves taking the $x_1$ (or $x_3$) Fourier transform of the function to be differentiated, multiplying the result by $ik_1$ (or $ik_3$), where $k_1$ ($k_3$) is the wavenumber in the $x_1$ ($x_3$) direction, followed by inverse transformation to get the desired derivative. This method has the advantage that it handles the high-wavenumber components of the function precisely. Thus the use of the pseudospectral method in the $x_1$ and $x_3$ directions gives us the best possible resolution (with a given number of grid points) in these directions. Partial derivatives in the $x_2$ direction were approximated by central-difference formulae. These will be described below.

The time advancement was made using a semi-implicit method (Moin *et al.* 1978). The momentum equations (2.6) were recast in the form

$$\frac{\partial \bar{u}_i}{\partial t} = -\frac{\partial P}{\partial x_i} + \left[(1+\delta_{i2})\langle \nu_T \rangle + \delta_{i1}\nu_T^* + \frac{1}{Re_\tau}\right]\frac{\partial^2 \bar{u}_i}{\partial x_2^2} + \frac{1}{Re_\tau}\left(\frac{\partial^2 \bar{u}_i}{\partial x_1^2} + \frac{\partial^2 \bar{u}_i}{\partial x_3^2}\right) + H_i \quad \text{(no summation)}, \tag{5.1}$$

where $H_i$ contains all of the terms in (2.6) that are not in (5.1). For discretization in time, we used the Adams–Bashforth method for $H_i$ and the Crank–Nicolson method for the remaining terms in the right-hand side of (5.1). For convenience, we evaluated $\langle \nu_T \rangle$ and $\nu_T^*$ at the old time step $n$.

In (5.1), $H_i$ includes the term

$$\epsilon_{ijk}\bar{u}_j\bar{\omega}_k + \frac{\partial}{\partial x_j}\tfrac{1}{2}\bar{u}_j\bar{u}_j.$$

The computation of this term can be accomplished by first calculating the term under

the large overbar, taking the Fourier transform with respect to $x_1$ and $x_3$, multiplying by the Fourier transform of the Gaussian filter function, and then inverse-transforming.

Next, we Fourier-transform the resulting equations in the $x_1$ and $x_3$ directions. This converts the set of partial differential equations (5.1) to the following system of ordinary differential equations, for every pair of Fourier modes $k_1$ and $k_3$ with $y = x_2$ as the independent variable:

$$\frac{\partial^2 \hat{u}_1^{n+1}}{\partial y^2} + \beta_1 \left[1 + \frac{\Delta t}{2Re}(k_1^2 + k_3^2)\right] \hat{u}_1^{n+1} + \tfrac{1}{2} i k_1 \beta_1 \Delta t \hat{P}^{n+1} = \hat{Q}_1, \tag{5.2a}$$

$$\frac{\partial^2 \hat{u}_2^{n+1}}{\partial y^2} + \beta_2 \left[1 + \frac{\Delta t}{2Re}(k_1^2 + k_3^2)\right] \hat{u}_2^{n+1} + \tfrac{1}{2} \beta_2 \Delta t \frac{\partial \hat{P}^{n+1}}{\partial y} = \hat{Q}_2, \tag{5.2b}$$

$$\frac{\partial^2 \hat{u}_3^{n+1}}{\partial y^2} + \beta_3 \left[1 + \frac{\Delta t}{2Re}(k_1^2 + k_3^2)\right] \hat{u}_3^{n+1} + \tfrac{1}{2} i k_3 \beta_3 \Delta t \hat{P}^{n+1} = \hat{Q}_3. \tag{5.2c}$$

Here $\beta_i\,(i = 1, 2, 3)$ are known functions of $Re_\tau$, $\langle \nu_T \rangle^n$, and $\nu_T^{*n}$, and $\hat{Q}_i$ represent the terms involving pressure and velocity field at time steps $n$ and $n-1$.

The central-difference formulae

$$\left.\frac{\partial^2 f}{\partial y^2}\right|_j \simeq 2\left[\frac{f_{j-1}}{h_j(h_j + h_{j+1})} - \frac{f_j}{h_j h_{j+1}} + \frac{f_{j+1}}{h_{j+1}(h_j + h_{j+1})}\right], \tag{5.3a}$$

$$\left.\frac{\partial f}{\partial y}\right|_q \simeq \frac{f_{q+1} - f_q}{y_{q+1} - y_q}, \tag{5.3b}$$

were used to approximate

$$\frac{\partial^2 \hat{u}_i^{n+1}}{\partial y^2}, \quad \frac{\partial \hat{P}^{n+1}}{\partial y}$$

respectively, in (5.2). Here $j$ denotes the velocity mesh point $y_j$, $q$ the pressure mesh point $y_q$, and $h_j = y_j - y_{j-1}$. The resulting set of equations, together with the equation of continuity evaluated at the pressure node points,

$$\tfrac{1}{2} i k_1 (\hat{u}_{1,j+1}^{n+1} + \hat{u}_{1,j}^{n+1}) + \frac{\hat{u}_{2,j+1}^{n+1} - \hat{u}_{2,j}^{n+1}}{h_{j+1}} + \tfrac{1}{2} i k_3 (\hat{u}_{3,j+1}^{n+1} + \hat{u}_{3,j}^{n+1}) = 0, \tag{5.4}$$

leads to a system of algebraic equations for the Fourier transform of the dependent variables at the new time step. This system is of block-tridiagonal form and can be solved very efficiently (see below). No-slip boundary conditions on velocity were used at the walls ($y = \pm 1$), and periodic boundary conditions were incorporated in the $x_1$ and $x_3$ directions. Note that pressure wall conditions are not necessary; only velocity boundary conditions are sufficient to close the system of equations (see Moin & Kim 1980).

In the present calculations, the core memory of the ILLIAC IV is large enough to hold only a few planes of the dependent variables. Therefore it is important to manage efficiently the transfer of data between the core and disk memory, where the entire data base resides. A detailed description of the data-management technique used here is given in Kim & Moin (1979). Here, we briefly outline the essential steps. At each time step, the system of algebraic equations just described is solved by two separate passes through the data base. In PASS 1, the right-hand side of these equations is computed. This is accomplished by transferring two $(x, z)$-planes of the independent variables

from the disk memory to the core memory to be processed by a double-buffer scheme. In this manner, all the $(x, z)$-planes are transferred to the core, two planes at a time.

In PASS 2, the block-tridiagonal system must be solved for each $k_1$ and $k_3$. In this pass, $(y, k_3)$-planes of the right-hand side vector that were computed in PASS 1 are transferred to the core memory. Owing to the limitation of the core size of the ILLIAC IV, a special algorithm had to be developed to solve the block-tridiagonal system of equations. For each $k_1$ and $k_3$, this algorithm requires $676N_2$ floating-point arithmetic operations, in contrast to $376N_2$ operations for the conventional block-tridiagonal solver (Merriam 1978 private communication). The extra computations are necessary in order to avoid the extra I/O passes that would otherwise have been necessary.

With a full use of the parallel processing capabilities of the ILLIAC IV computer and the above data-management technique, the computer time per time step (CPU and I/O time) was 22 s for $63 \times 64 \times 64$ grid-point calculations and 36 s for the computations with $63 \times 64 \times 128$ grid points. For the calculations shown in table 1, the dimensionless time step $\Delta t$ was set at 0·001 for case 1, 0·000 75 for case 2, and 0·0005 for cases 3 and 4. The total time of calculation on the ILLIAC IV was approximately 24 h for case 1, 48 h for case 2, 78 h for case 3, and 92 h for case 4. Throughout the computations, the value of

$$C(t) = \max\left\{\Delta t\left[\left|\frac{\bar{u}}{h_1}\right| + \left|\frac{\bar{v}}{h_2(y)}\right| + \left|\frac{\bar{w}}{h_3}\right|\right]\right\}$$

never exceeded 0·35.

The initial condition for case 1 in table 1 was obtained by assigning the final velocity field described in Kim & Moin (1979) to the corresponding grid points used here. For case 2, the final velocity field from case 1 was simply assigned to the alternate mesh points. The values at the intermediate points were obtained by Fourier interpolation. A similar procedure was used to generate the initial velocity field for cases 3 and 4.

## 6. Mean-velocity profile and turbulence statistics

Starting from the initial velocity field, for each case, the governing equations were integrated forward in time until the numerical solutions reached statistically steady states. These equilibrium states were identified by approximate periodicity of the horizontally averaged turbulence stresses in time. Next, in order to obtain better statistical samples, the equations were further integrated in time, and a running time average of the horizontally averaged turbulence quantities was calculated. For each case, the calculations were considered to be complete when the time-averaged turbulence quantities became stationary. The total time of integration and the averaging time for all the computations reported here are shown in table 1.

Figure 1 shows the mean-velocity profile $\langle \bar{u} \rangle$ (unless otherwise stated, in this section $\langle\ \rangle$ indicates horizontal as well as time averaging) for all cases reported in table 1. The calculated mean-velocity profiles are in good agreement with each other as well as with the experimental data of Hussain & Reynolds (1975). It appears that, at least for the different computational grid networks considered here, the law of the wall and the corresponding logarithmic layer and von Kármán constant can be predicted with virtually no dependence on the grid resolution. This is particularly significant in light of the fact that the characteristic length scale of the subgrid-scale model used here is a function of computational grid resolution. Figure 2 shows the profiles of the correlation

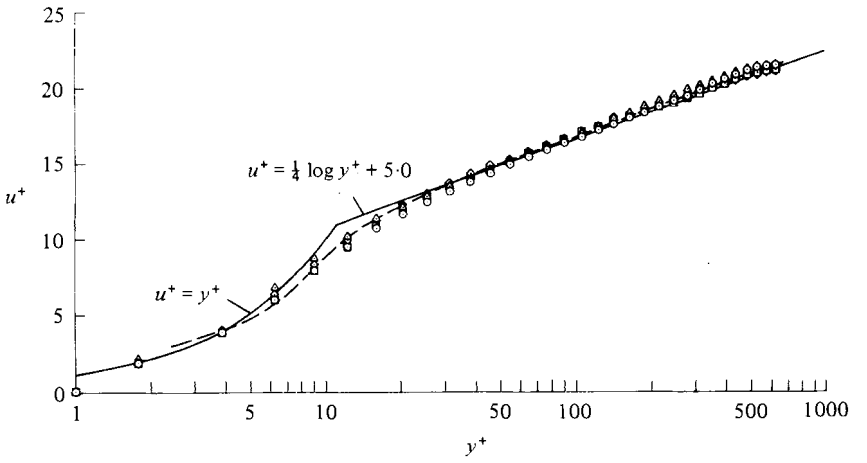


FIGURE 1. Mean-velocity profiles from four computed cases and comparison with experimental data: — — —, Hussain & Reynolds (1975), $Re$ = 13800; △, case 1; ◇, 2; □, 3; ○, 4.

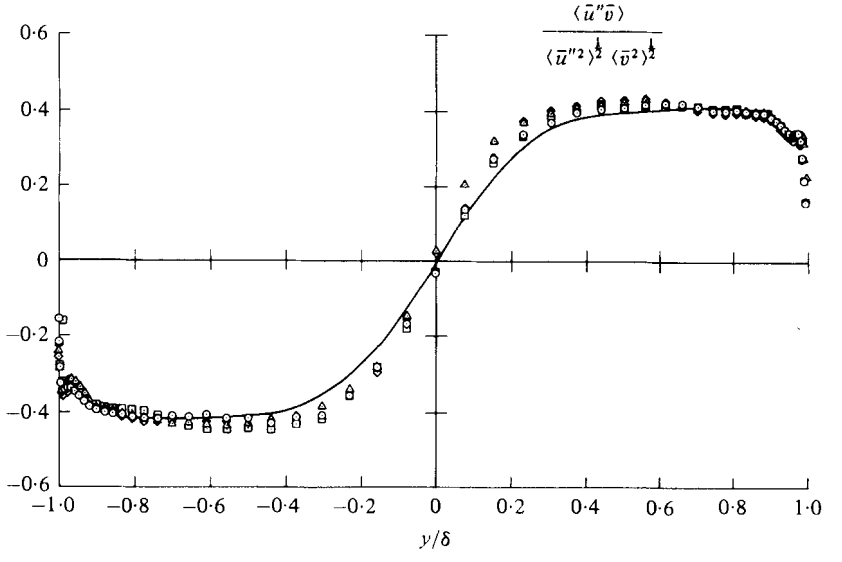


FIGURE 2. Correlation coefficients between $\bar{u}''$ and $\bar{v}$ from four computational cases and comparison with experimental data: ———, Sabot & Comte-Bellot (1976); △, case 1; ◇, 2; □, 3; ○, 4.

coefficient between the resolvable streamwise and vertical components of turbulent fluctuations,

$$\langle \bar{u}''\bar{v} \rangle / [\langle \bar{u}''^2 \rangle^{\frac{1}{2}} \langle \bar{v}^2 \rangle^{\frac{1}{2}}],$$

where $\bar{u}'' = \bar{u} - \langle \bar{u} \rangle$. The calculated profiles for all the cases reported in table 1 are in good agreement with each other and with the experimental data of Sabot & Comte-Bellot (1976). The results presented in figure 2 together with those in figure 1 establish some confidence in the reliability of the subgrid-scale model used in this study.

In the remainder of this paper we shall present, in some detail, the results obtained from case 4 in table 1. The computational grid resolution for this case is better than for all the other cases; and, as will be shown later in this section, the computational domain appears to be large enough to include the important large eddies.

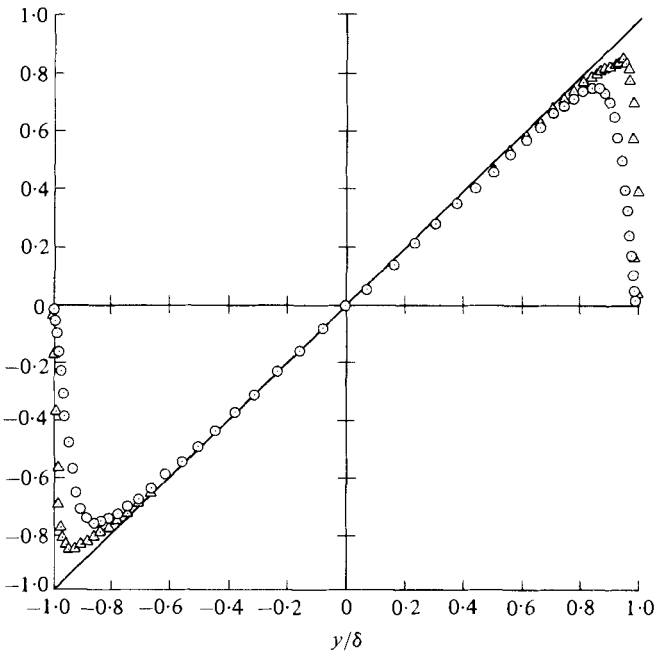


FIGURE 3. Resolvable and total turbulence shear stress: ○, $\langle \bar{u}''\bar{v} \rangle$; △, $\langle \bar{u}''\bar{v} \rangle + \tau_{12}$.

### 6.1. *Turbulence stresses*

Vertical profiles of the resolvable mean Reynolds shear stress $\langle \bar{u}''\bar{v} \rangle$ and the total Reynolds shear stress $\langle \bar{u}''\bar{v} \rangle + \langle \tau_{12} \rangle$ are shown in figure 3. These profiles indicate that the average Reynolds shear-stress profile has attained the equilibrium shape that balances the downstream mean pressure gradient in the regions away from the walls. In the vicinity of the walls, the viscous stresses are significant, and they, together with the total Reynolds stress, balance the mean pressure gradient. The symmetry of the $|\langle \bar{u}''\bar{v} \rangle + \tau_{12}|$ profile about the channel centre line indicates that the total averaging time and statistical sample are adequate. Moreover, it should be noted that the subgrid-scale contribution to the total Reynolds stress is significant only in the vicinity of the walls.

Figures 4 and 5 show the profiles of the dimensionless resolvable turbulence intensities. For comparison, some of the available experimental data over a range of Reynolds numbers are also shown. Once again, the symmetry of the calculated turbulence intensities about the centre line of the channel indicates that the total averaging time was sufficient for an adequate statistical sample. The overall agreement of the computed turbulence intensities with the experimental measurements is good. In figure 5, the resolvable turbulence intensities in the vicinity of the lower wall are plotted *vs.* $y^+ = y_w u_\tau / \nu$. In spite of large differences among various measurements, the maximum of the computed $\langle \bar{u}''^2 \rangle^{\frac{1}{2}}$ is located at a distance farther away from the wall ($y^+ \simeq 30$) than those of the measured turbulence intensities ($y^+ \simeq 13$–$20$). In addition, in the immediate neighbourhood of the wall, an appreciable fraction of the vertical component of turbulence intensity appears to reside in the subgrid-scale motions. It should be noted that, in contrast to the turbulence shear stress, in order to deduce the subgrid-scale contribution to turbulence intensities one has to obtain an estimate for the

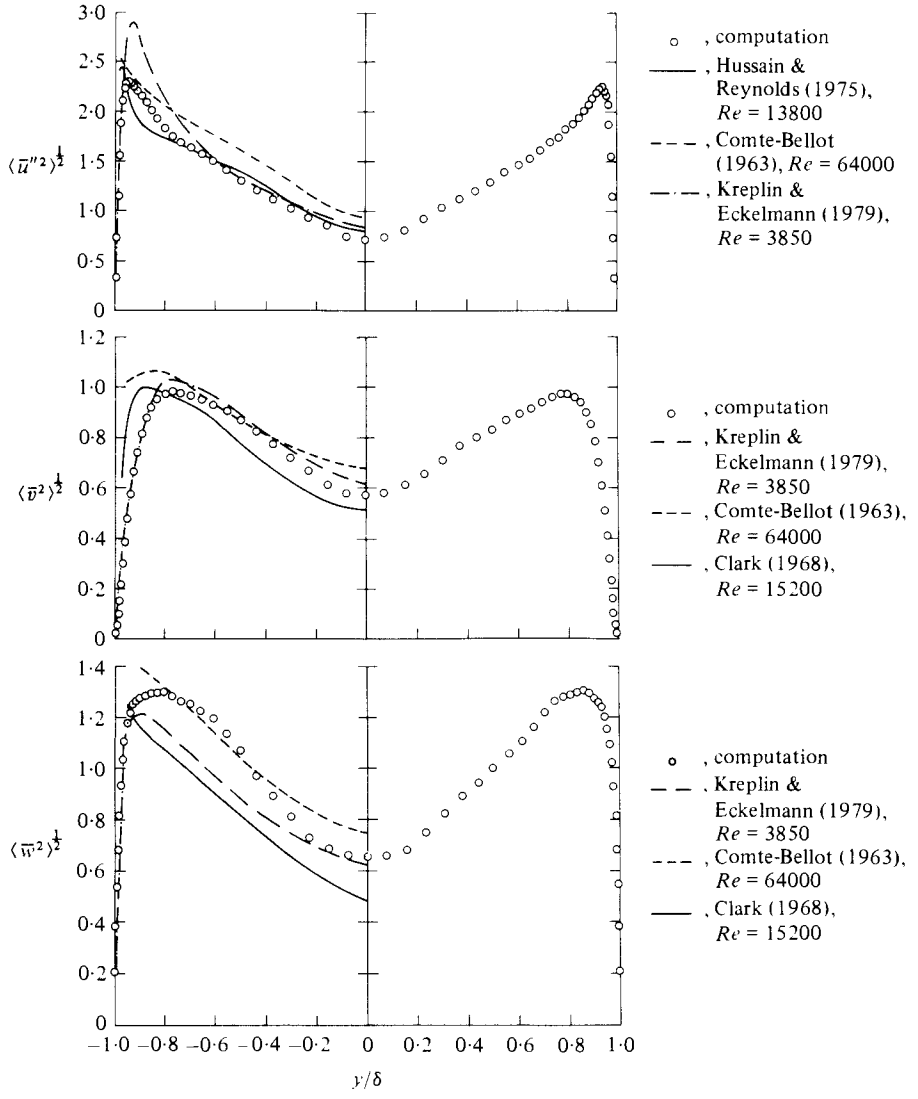


FIGURE 4. Resolvable turbulence intensities and comparison with experimental data.

kinetic energy of SGS stress $Q_{kk}$, and use it in (2.8$a$). Owing to the high degree of anisotrophy in the channel flow, especially in the vicinity of the walls, we have been unable to obtain a reasonably accurate estimate for $Q_{kk}$.

### 6.2. *Two-point correlation functions*

Two-point correlation functions

$$R_{ii}(y, r_1) = \frac{\langle \bar{u}_i''(x, y, z)\, \bar{u}_i''(x + r_1, y, z) \rangle}{\langle \bar{u}_i''^2(x, y, z) \rangle},$$

$$R_{ii}(y, r_3) = \frac{\langle \bar{u}_i''(x, y, z)\, \bar{u}_i''(x, y, z + r_3) \rangle}{\langle \bar{u}_i''^2(x, y, z) \rangle}$$

for $i = 1, 2, 3$ (no summation) are plotted in figures 6 and 7 at four vertical locations. These profiles show that, in general, for small separation distances, the correlation for

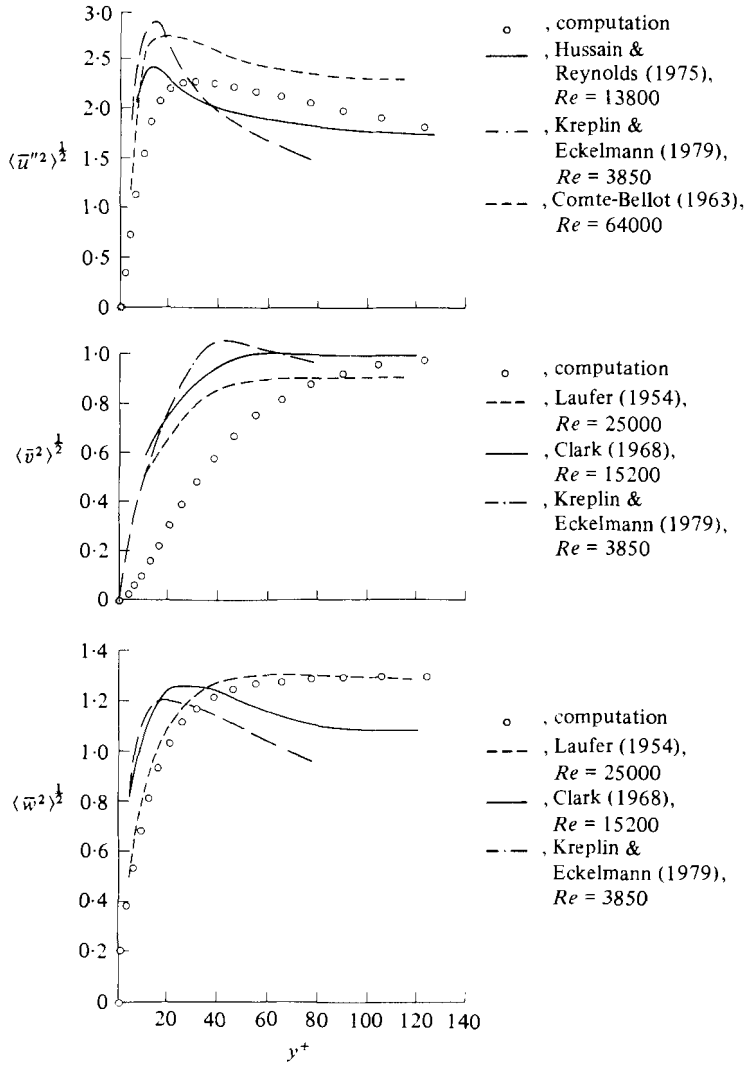


FIGURE 5. Resolvable turbulence intensities in the vicinity of the lower wall and comparison with experimental data.

the velocity in the direction of the displacement is larger than the corresponding transverse correlations. In addition, the longitudinal correlation in the streamwise direction extends over much longer distances than do all other correlations. This result was also obtained by Deardorff (1970).

The slow decay of $R_{11}(y_w = 0{\cdot}025, r_1)$ for increasing $r_1$ indicates that near the wall the eddies are highly elongated in the streamwise direction. On the other hand, the profiles of $R_{11}(y, r_3)$ show that the spanwise extent of turbulence structures near the wall is much smaller than for those away from the wall. Thus, it appears that, in accordance with the experimental observations, near the walls the computed flow field consists of elongated streaky structures. The structure of the flow field will be examined in some detail in §7.

For comparison, in figures 6 and 7, the profiles of $R_{11}(y_w, r_i)$ $(i = 1, 3)$ at $y_w/\delta = 0{\cdot}11$,

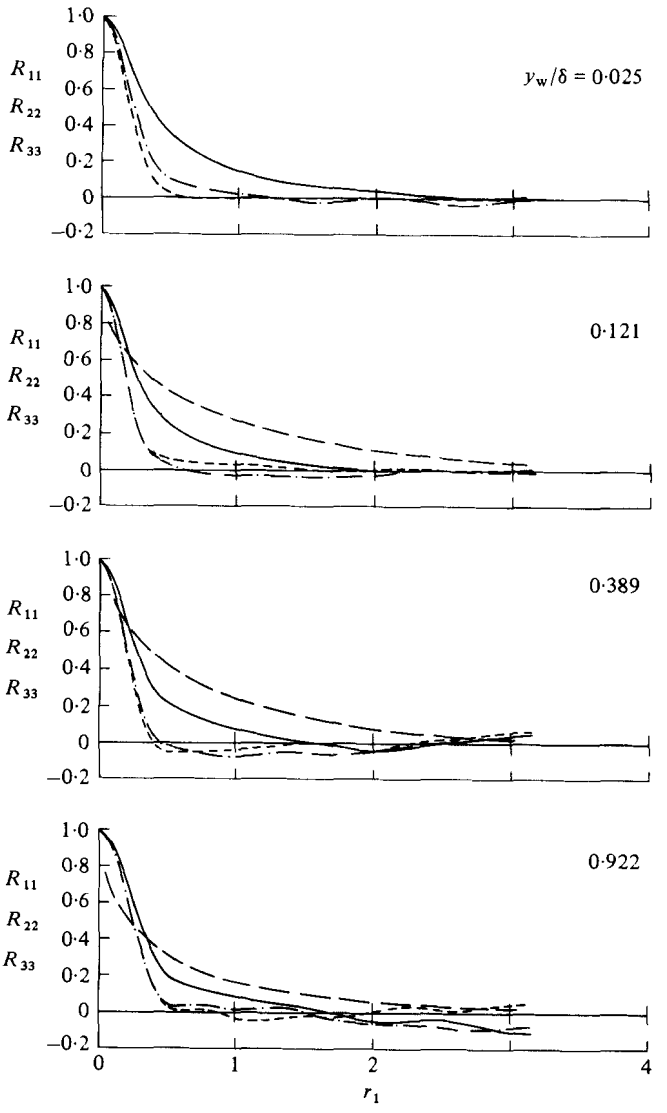


FIGURE 6. Streamwise two-point correlation function. ——, $R_{11}$; – – – –, $R_{22}$; — · —, $R_{33}$; — — —, $R_{11}$, Comte-Bellot (1963).

0·44, and 1·0 from Comte-Bellot's (1963) measurements are included. Note that the computed and measured correlations are obtained at slightly different vertical locations. The correlations were calculated at selected points in the $y$-direction, and the comparison is made at the locations where the $y$-co-ordinates of the computed and measured correlations were closest to each other. For small values of the non-dimensionalized separation distance $r_1$, the measured correlations $R_{11}(y_w, r_1)$ are smaller than the computed ones, whereas for larger values of $r_1$ the reverse is true. At small values of $r_1$, the discrepancy between the computed and measured correlations is due to the fact that the measurements were made at a much larger Reynolds number ($Re$ = 135000) than in the present simulation (see Batchelor 1953). However, the cause of the difference between the computed and measured profiles for larger values of $r_1$ is

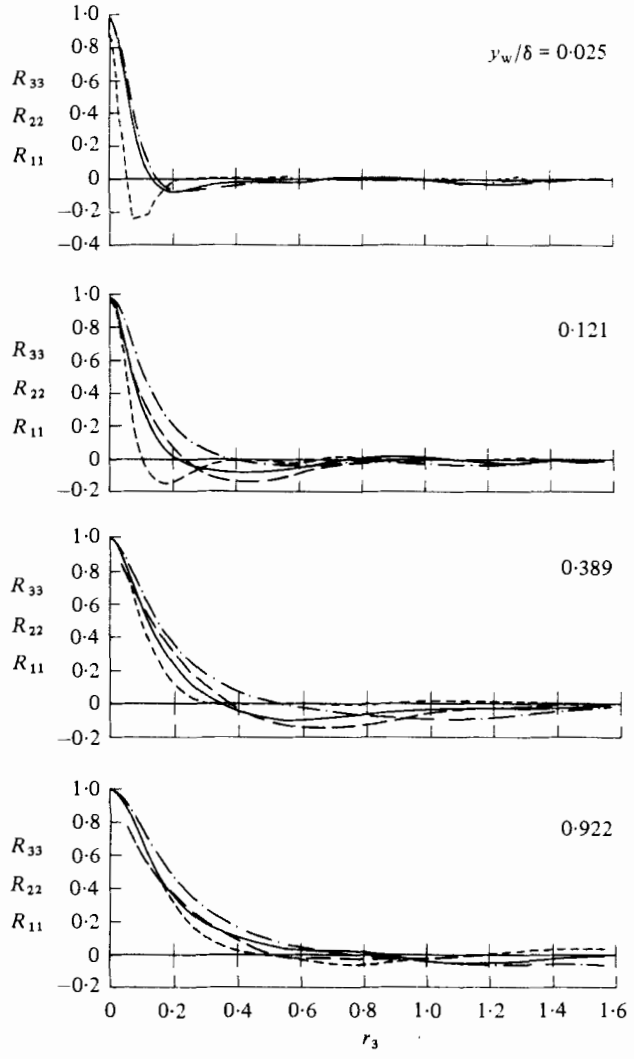


FIGURE 7. Spanwise two-point correlation function. ——, $R_{11}$; – – – –, $R_{22}$; —·—, $R_{33}$; ———, $R_{11}$, Comte-Bellot (1963).

not clear. Comparison of the measured profiles with the computed ones obtained from calculations with larger computational box lengths in the streamwise direction shows no improvement. Thus the streamwise extent of the computational box does not appear to be a factor here. However, possible inadequate resolution in the $x$-direction may suppress the formation of some small-scale structures. In this case, these structures could conceivably combine to form eddies that have long streamwise extent through the channel cross-section. In addition, it should be mentioned that Comte-Bellot's axial two-point correlation data were obtained by traversing one probe downstream of another probe. With this procedure, the measured $R_{11}(y, r_1)$ may be contaminated with errors due to the effect of the wake of the upstream probe. However, the probe interference effect should be significant only for small separation distances.

In figure 7, the profiles of $R_{11}(y, r_3)$ are also compared with the measurements of

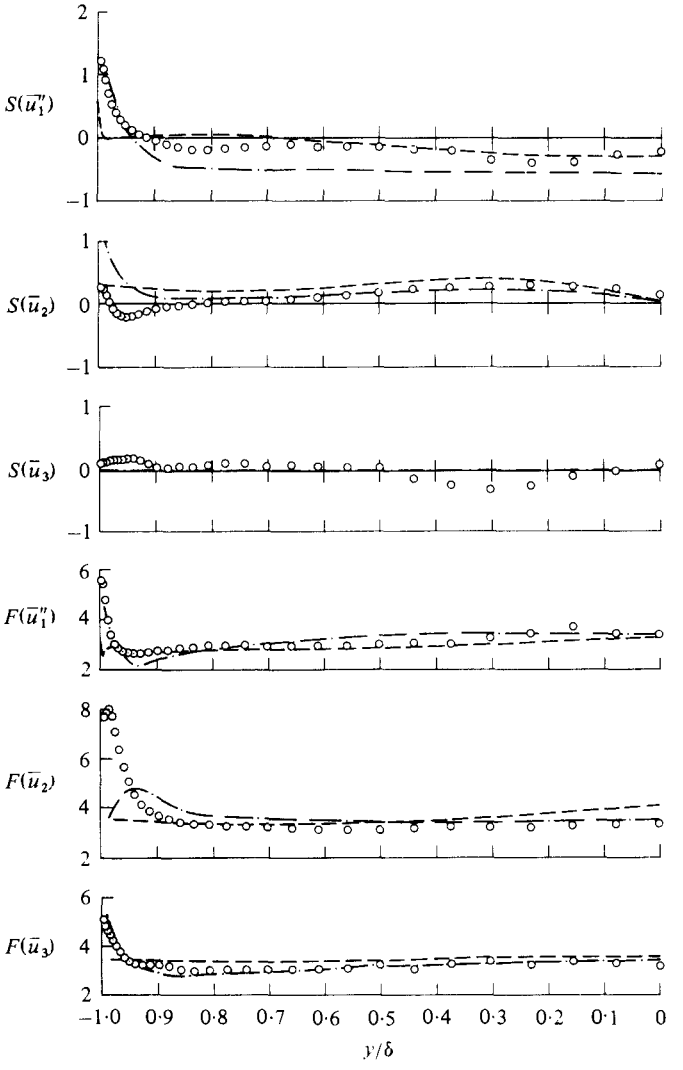


FIGURE 8. Skewness and flatness factors. ⊙, computation; —·—, Kreplin & Eckelmann (1979); — — — —, Comte-Bellot (1963).

Comte-Bellot. Aside from the Reynolds-number effect for small values of $r_3$, the agreement between the computed and measured correlations is good. Finally, the other two spanwise correlations $R_{22}(y, r_3)$ and $R_{33}(y, r_3)$ were also compared with the corresponding ones measured by Comte-Bellot. The measured $R_{22}(y, r_3)$ and $R_{33}(y, r_3)$ are systematically lower than the computed ones for the values of $r_3$ for which these correlations have appreciable magnitude.

### 6.3. *Skewness and flatness factors of resolvable turbulence*

The velocity skewness and flatness factors, which are defined as

$$S(\bar{u}_i'') = \frac{\langle \bar{u}_i''^3 \rangle}{\langle \bar{u}_i''^2 \rangle^{\frac{3}{2}}}, \quad F(\bar{u}_i'') = \frac{\langle \bar{u}_i''^4 \rangle}{\langle \bar{u}_i''^2 \rangle^2} \quad (i = 1, 2, 3; \text{ no summation})$$

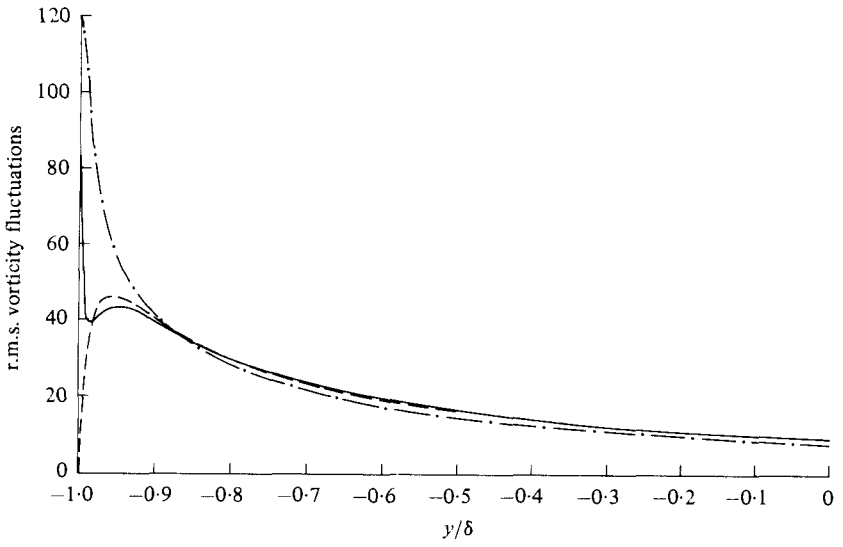


FIGURE 9. Resolvable root-mean square vorticity fluctuations: ———, $\langle \omega_1^2 \rangle^{\frac{1}{2}}$; – – – –, $\langle \omega_2^2 \rangle^{\frac{1}{2}}$; —·—, $\langle \omega_3''^2 \rangle^{\frac{1}{2}}$.

respectively, are plotted in figure 8. The flatness factors of all the velocity components reach their maxima at the wall. This indicates that in the vicinity of the wall the turbulence is highly intermittent. Throughout an appreciable portion of the channel cross-section, $F(\bar{u}_3)$ and $S(\bar{u}_3)$ are approximately equal to three and zero respectively. These values correspond to the flatness and skewness factors of a Gaussian distribution. However, Kreplin & Eckelmann (1979) measured the $u_3$ probability distribution and have shown that it is not Gaussian, even though the values of $S(u_3)$ and $F(u_3)$ correspond to that of a Gaussian distribution.

Near the wall, $S(\bar{u}_1'')$ is positive, whereas away from the wall it is negative. This indicates that near the wall the large-amplitude $\bar{u}$-fluctuations are due primarily to arrival of high-speed fluid from regions away from the wall. On the other hand, away from the wall the large-amplitude $\bar{u}$-fluctuations are most probably associated with low-speed fluid leaving the wall region. These observations are in agreement with the experimental findings of Brodkey, Wallace & Eckelmann (1974), and with contour plots of $\bar{u}''\bar{v}$ from numerical simulation of turbulent channel flow (Kim & Moin 1979). However, as will become clear below, the precise vertical location (in wall units) of the crossover point in the present calculation is in disagreement with experimental data. This discrepancy is probably due to inadequate grid resolution in the computations.

In figure 8, the profiles of skewness and flatness factors from measurements of Comte-Bellot (1963) and Kreplin & Eckelmann (1979) are reproduced. The overall agreement between computational and experimental data is good. This is particularly encouraging considering the significant contribution of small-scale turbulence to these quantities and the difficulties associated with their measurements.

### 6.4. *Resolvable vorticity fluctuations*

Figure 9 shows the profiles of the non-dimensional r.m.s. vorticity fluctuations. The spanwise component of vorticity fluctuations $\langle \omega_3''^2 \rangle^{\frac{1}{2}}$ attains its maximum at the wall, and decreases monotonically towards the channel centre line. The profile of the r.m.s.

streamwise vorticity fluctuations $\langle\omega_1^2\rangle^{\frac{1}{2}}$ also attains its maximum at the wall, but, in addition, displays a local maximum at $y^+ \simeq 30$. At about the same location, the peak of the r.m.s. vertical component of the vorticity is located. The mechanics underlying this behavior of the profile of $\langle\omega_1^2\rangle^{\frac{1}{2}}$ will be discussed in §7.

It is interesting to note that, in spite of large differences between different components of r.m.s. $\langle\omega_i''^2\rangle^{\frac{1}{2}}$ near the wall, away from the wall ($y^+ > 70$) they are virtually identical. This is in contrast to r.m.s. velocity fluctuations $\langle\bar{u}_i''^2\rangle^{\frac{1}{2}}$. The difference between the two may be explained by noting that the relative contribution of small scales to vorticity fluctuations is significantly larger than their contribution to velocity fluctuations, and away from the walls the small scales tend to be isotropic. Exploiting the 'isotropy' of vorticity fluctuations may be very useful in statistical analysis of turbulent shear flows.

The limiting wall values of vorticity fluctuations in the present calculations are $0{\cdot}20\langle\partial\bar{u}_1/\partial y\rangle$ and $0{\cdot}13\langle\partial\bar{u}_1/\partial y\rangle$ for $\langle\omega_3''^2\rangle^{\frac{1}{2}}$ and $\langle\omega_1^2\rangle^{\frac{1}{2}}$ respectively. The agreement of these computed values with experimental measurements (see Kreplin & Eckelmann (1979) for data from several measurements) is satisfactory.

### 6.5. *Statistics involving resolvable pressure fluctuations*

The root-mean-square value of the resolvable wall-pressure fluctuations $\langle P^2\rangle^{\frac{1}{2}}/\tau_w$ is 2·05 for both walls. This value is in fair agreement with the values of 2·64 obtained by Willmarth & Wooldridge (1962), 2·31 by Willmarth (1965), 2·6 by Elliott (1972), and of 2·0 and 2·5 reported by Corcos (1962) for fully developed pipe flows. However, the computed values are considerably lower than the 3·59 obtained by Blake (1970) or Emmerling's (1973) measurements (see Willmarth 1975). There is strong evidence (Willmarth 1975) that the contribution of small-scale fluctuations to the intensity of wall-pressure fluctuations is significant. The measurements of Blake and Emerling were made respectively with a pinhole microphone and by optical techniques. Therefore, in these experiments the smaller-scale pressure variations are expected to be better resolved. Thus, in view of these two experiments, it appears that an appreciable portion of the pressure fluctuations may reside in subgrid-scale motions. However, there is some indication that the intensity of the large-scale wall-pressure fluctuations increases with Reynolds number (Willmarth 1975). Since the above measurements were made at higher Reynolds numbers than the present simulation, some of the discrepancy between the computations and latter two experiments may be due to the difference in Reynolds number.

The profiles of the diagonal elements of the *resolvable* pressure–strain correlation tensor

$$\phi_{ij} = \left\langle P\left(\frac{\partial\bar{u}_i}{\partial x_j} + \frac{\partial\bar{u}_j}{\partial x_i}\right)\right\rangle$$

are shown in figures 10 and 11. These terms govern the exchange of energy between the three components of resolvable turbulence kinetic energy (Hinze 1975). The negative sign for $\phi_{ll}$ (no summation) indicates loss, or transfer of energy from $\langle\bar{u}_l''^2\rangle^{\frac{1}{2}}$ to other components, whereas a positive sign denotes energy gain. These profiles show that, except in the close vicinity of the wall, as expected, the streamwise component of turbulent velocity fluctuations transfers energy to the cross-stream components. However, very near the wall, there is a large transfer of energy from the vertical

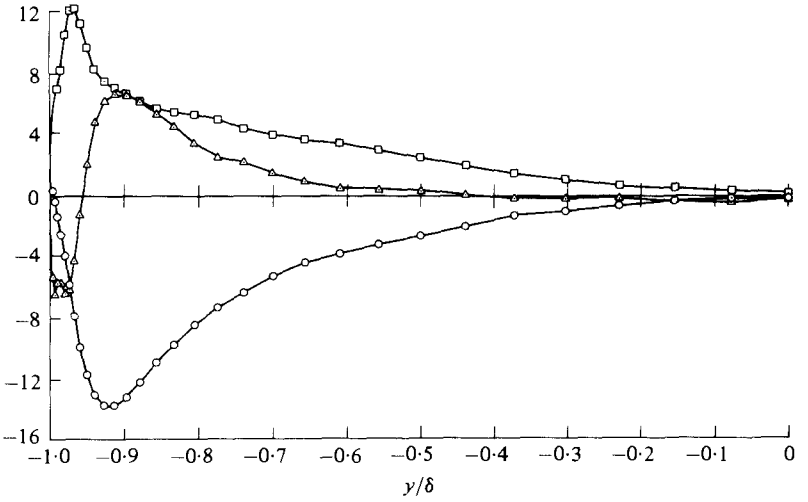


FIGURE 10. Resolvable portion of the trace of the pressure–strain correlation tensor: ○, $\phi_{11}$; △, $\phi_{22}$; □, $\phi_{33}$.

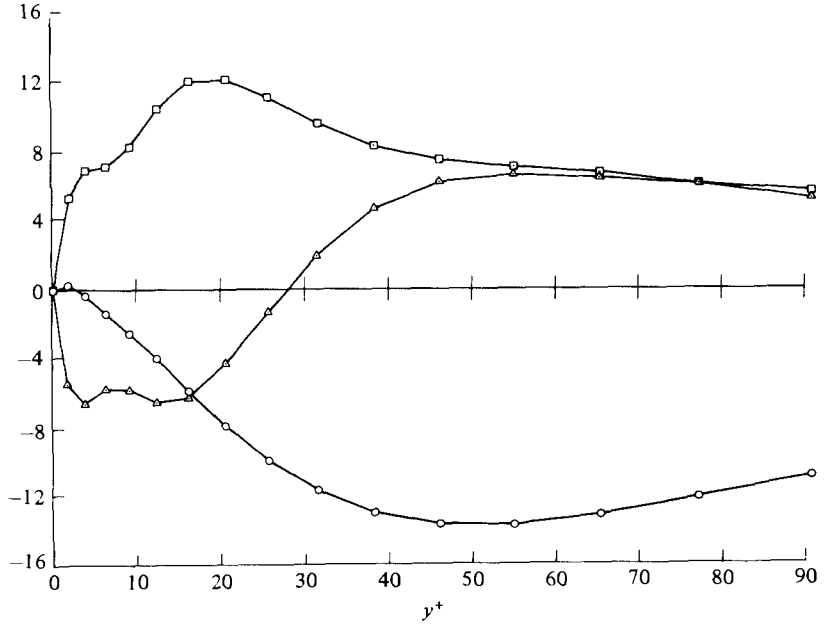


FIGURE 11. Resolvable portion of the trace of the pressure–strain correlation tensor in the vicinity of the lower wall: ○, $\phi_{11}$; △, $\phi_{22}$; □, $\phi_{33}$.

component of turbulence intensity to the horizontal components. In this work, we shall refer to this phenomenon as the 'splatting' or impingement effect. This effect will be discussed further in §7. It will be shown that the splatting effect is an important property of the flow in the vicinity of the walls, and should be taken into account in the modelling of near-wall turbulence. In fact, this phenomenon was noted in a previous study by Daly & Harlow (1970), who included a term in their statistical model of $\phi_{ij}$ to account for its effect.

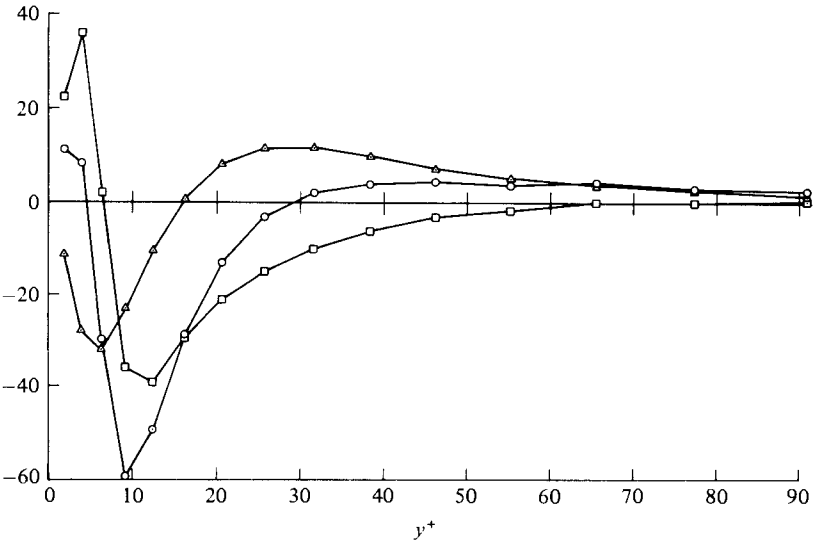


FIGURE 12. Resolvable portion of the off-diagonal element of the pressure–strain correlation tensor $\phi_{12}$ (△), pressure-diffusion term $-\partial\langle P\bar{u}''\rangle/\partial y$ (□), and their sum $P_{uv}$ (○), where $P_{uv} = -\langle \bar{u}''\,\partial P/\partial y + \bar{v}\,\partial P/\partial x\rangle$.

The profile of the off-diagonal element $\phi_{12}$, together with the pressure diffusion term $-\partial\langle P\bar{u}''\rangle/\partial y$, and their sum

$$P_{uv} = -\left\langle \bar{u}''\frac{\partial P}{\partial y} + \bar{v}\frac{\partial P}{\partial x}\right\rangle$$

in the vicinity of the lower wall are shown in figure 12. The last term $P_{uv}$ appears in the governing equation for resolvable turbulence shear stress, $\langle \bar{u}''\bar{v}\rangle$. The components of $P_{uv}$, $\phi_{12}$, and $-\partial\langle P\bar{u}''\rangle/\partial y$, have comparable magnitudes, and, as will be shown below, near the wall they provide important contributions to the governing equation for $\langle \bar{u}''\bar{v}\rangle$. As expected (Hinze 1975), except in the immediate neighbourhood of the wall, the sign of $\phi_{12}$ is opposite to that of $\langle \bar{u}''\bar{v}\rangle$. However, near the wall, where the splatting effect is present, $\phi_{12}$ has the same sign as $\langle \bar{u}''\bar{v}\rangle$, thus contributing to the production of turbulence.

### 6.6. *Resolvable turbulence intensity and shear-stress balance*

In phenomenological turbulence modelling, the objective is to construct rational models for the correlations that appear in the governing equations for the Reynolds stresses. For the *resolvable* portion of the flow field in channel flow, these equations are

$$\frac{\partial\langle \bar{u}_1''^2\rangle}{\partial t} = -\langle \bar{u}_1''\bar{u}_2\rangle\frac{\partial\langle \bar{u}_1\rangle}{\partial x_2} - \frac{\partial}{\partial x_2}\langle \bar{u}_1''^2\bar{u}_2\rangle - 2\left\langle \bar{u}_1''\frac{\partial P}{\partial x_1}\right\rangle$$
$$+\frac{\partial}{\partial x_2}\left\langle\left(\nu_T + \frac{1}{Re_\tau}\right)\frac{\partial \bar{u}_1''^2}{\partial x_2}\right\rangle - 2\left\langle \bar{u}_1''\frac{\partial}{\partial x_j}\lambda_{1j}\right\rangle - 2\left\langle\left(\frac{1}{Re_\tau} + \nu_T\right)\frac{\partial \bar{u}_1''}{\partial x_j}\frac{\partial \bar{u}_1''}{\partial x_j}\right\rangle + A_{11}, \quad (6.1)$$

$$\frac{\partial\langle \bar{u}_2^2\rangle}{\partial t} = -\frac{\partial}{\partial x_2}\langle \bar{u}_2^3\rangle - 2\left\langle \bar{u}_2\frac{\partial P}{\partial x_2}\right\rangle + \frac{\partial}{\partial x_2}\left\langle\left(\nu_T + \frac{1}{Re_\tau}\right)\frac{\partial \bar{u}_2^2}{\partial x_2}\right\rangle$$
$$-2\left\langle \bar{u}_2\frac{\partial}{\partial x_j}\lambda_{2j}\right\rangle - 2\left\langle\left(\frac{1}{Re_\tau} + \nu_T\right)\frac{\partial \bar{u}_2}{\partial x_j}\frac{\partial \bar{u}_2}{\partial x_j}\right\rangle + A_{22}, \quad (6.2)$$

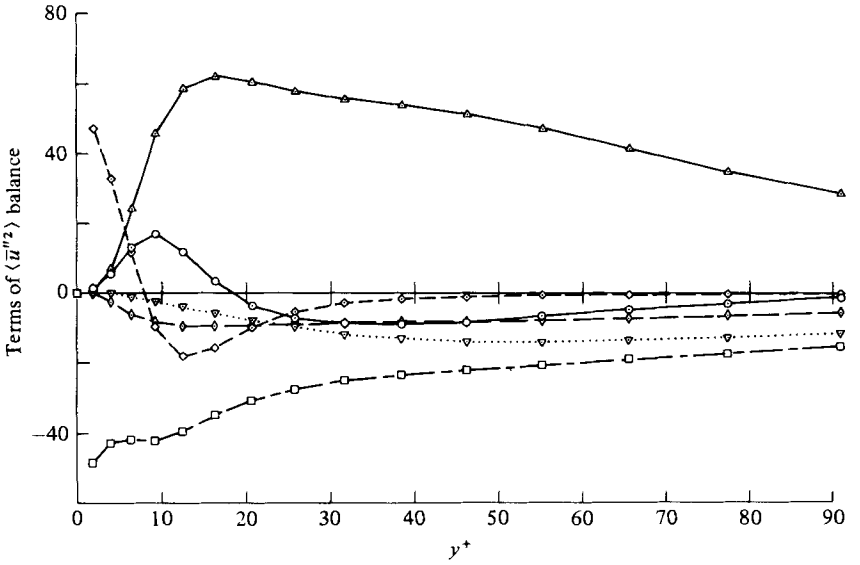


FIGURE 13. Balance of the resolvable portion of the streamwise component of turbulent kinetic energy: △, production; ⊙, convection (turbulent diffusion); ◇, cascade; ▽, velocity–pressure gradient; ⊡, dissipation; ◇, viscous diffusion.

$$\frac{\partial\langle\bar{u}_3^2\rangle}{\partial t} = -\frac{\partial}{\partial x_2}\langle\bar{u}_3^2\bar{u}_2\rangle - 2\left\langle\bar{u}_3\frac{\partial P}{\partial x_3}\right\rangle + \frac{\partial}{\partial x_2}\left\langle\left(\nu_T + \frac{1}{Re_\tau}\right)\frac{\partial\bar{u}_3^2}{\partial x_2}\right\rangle$$
$$- 2\left\langle\bar{u}_3''\frac{\partial}{\partial x_j}\lambda_{3j}\right\rangle - 2\left\langle\left(\frac{1}{Re_\tau} + \nu_T\right)\frac{\partial\bar{u}_3}{\partial x_j}\frac{\partial\bar{u}_3}{\partial x_j}\right\rangle + A_{33}, \tag{6.3}$$

$$\frac{\partial\langle\bar{u}_1''\bar{u}_2\rangle}{\partial t} = -\langle\bar{u}_2^2\rangle\frac{\partial\langle\bar{u}_1\rangle}{\partial y} - \frac{\partial}{\partial x_2}\langle\bar{u}_1''\bar{u}_2^2\rangle - \left\langle\bar{u}_1''\frac{\partial P}{\partial x_2} + \bar{u}_2\frac{\partial P}{\partial x_1}\right\rangle$$
$$+ \frac{\partial}{\partial x_2}\left\langle\left(\nu_T + \frac{1}{Re_\tau}\right)\frac{\partial\bar{u}_1''\bar{u}_2}{\partial x_2}\right\rangle - \left\langle\bar{u}_1''\frac{\partial}{\partial x_j}\lambda_{2j} + \bar{u}_2\frac{\partial}{\partial x_j}\lambda_{1j}\right\rangle$$
$$- 2\left\langle\left(\frac{1}{Re_\tau} + \nu_T\right)\frac{\partial\bar{u}_1''}{\partial x_j}\frac{\partial\bar{u}_2}{\partial x_j}\right\rangle + A_{12}. \tag{6.4}$$

It should be emphasized that the above equations are for the resolvable portion rather than the total turbulent stresses. However, considerable insight into the mechanics of energy transfer and the relative importance of various terms in the Reynolds-stress equations may be gained from the corresponding terms in these equations.

In figures 13–17, all the correlations appearing in the above equations, and in the governing equation for the resolvable turbulent kinetic energy, $q^2 = \frac{1}{2}\langle\bar{u}_1'' + \bar{u}_2^2 + \bar{u}_3^2\rangle$, are plotted in the vicinity of the lower wall ($y^+ < 90$). The first term in the right-hand side of (6.1) and (6.4) is the production term. In figures 13–17, the remaining five terms in the right-hand side of each equation are labelled as convection (turbulent diffusion), velocity–pressure gradient (VPG), diffusion, cascade, and dissipation. The last term in each equation, $A_{ij}$, is a relatively complicated expression involving $\nu_T$. They would be identically equal to zero if $\nu_T$ were a constant. These terms were calculated and found to be negligibly small compared with the other terms in each equation.

In figures 13 and 17, the production and dissipation are clearly the dominant terms in

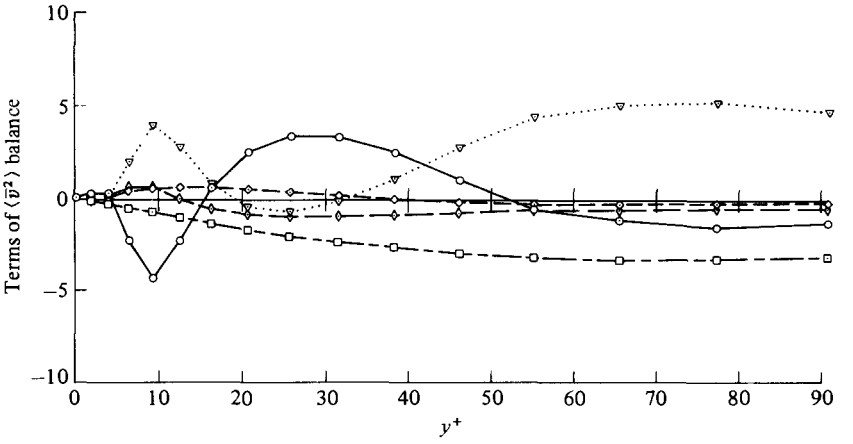


FIGURE 14. Balance of the resolvable portion of normal component of turbulent kinetic energy. See caption of figure 13 for details.

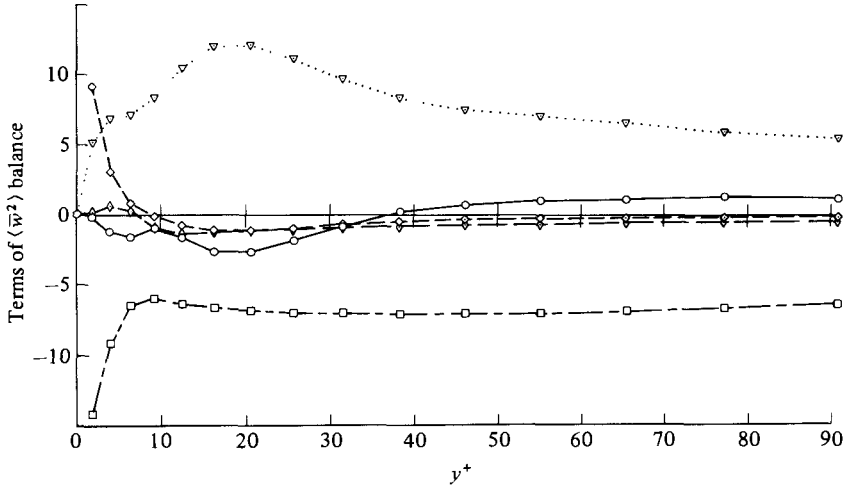


FIGURE 15. Balance of the resolvable portion of spanwise component of turbulent kinetic energy. See caption of figure 13 for details.

most of the region shown. In the immediate neighbourhood of the wall, however, where the production term is small, viscous diffusion carries sufficient energy inward to balance the large viscous dissipation there. In addition, it can be seen that, aside from the close vicinity of the wall ($y^+ < 15$), energy is convected from the wall region, where production is high, to the regions away from the wall.

The velocity–pressure-gradient terms make large contributions to the balance of the governing equations for normal and spanwise components of turbulent kinetic energy. Near the wall, the triple-correlation term (convection) and pressure–strain and pressure-diffusion terms in the $\langle \bar{u}_2^2 \rangle$ equation are very significant. In particular, the reduction of the normal component of turbulent energy due to the splatting effect mentioned above is compensated by the pressure-diffusion term.

Near the wall ($y^+ < 25$), in the dynamical equation for Reynolds shear stress $\langle \bar{u}''\bar{v} \rangle$, the triple-correlation and velocity–pressure gradient, $P_{uv}$, are the dominant

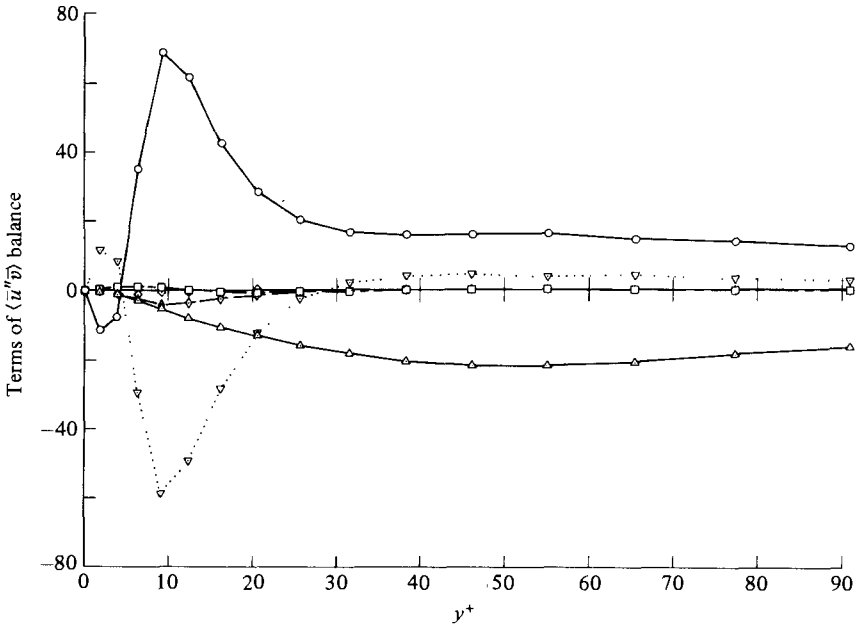


FIGURE 16. Balance of the resolvable portion of turbulence shear stress. See caption of figure 13 for details.

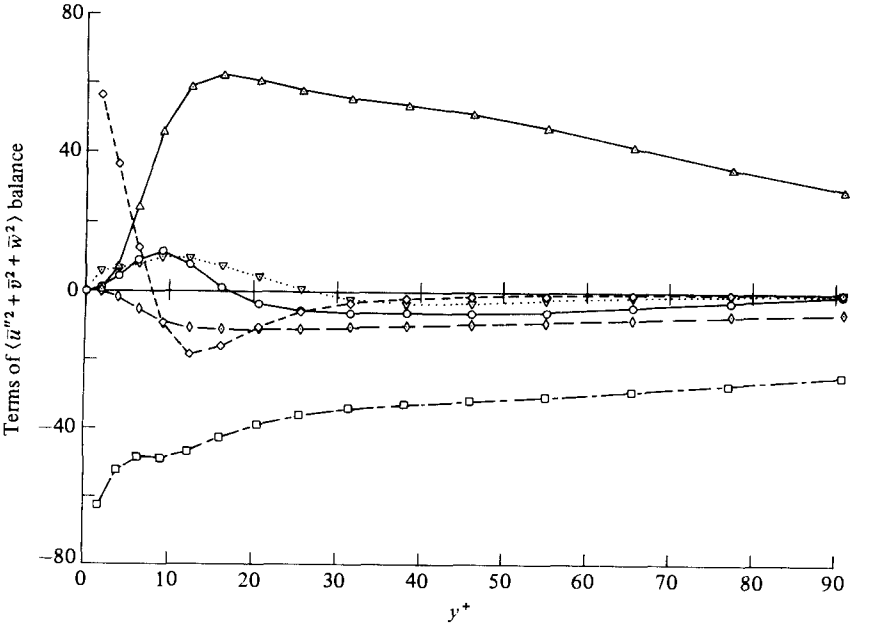


FIGURE 17. Balance of the resolvable turbulence kinetic energy. See caption of figure 13 for details.

terms. However, for $y^+ > 25$, the contribution of $P_{uv}$ is small and the production term takes on a more active role. Moreover, it should be noted that in this equation the viscous-diffusion and 'dissipation' terms appear to be negligible.

In (6.2)–(6.4) and in figures 13–17, the terms involving molecular and eddy viscosity

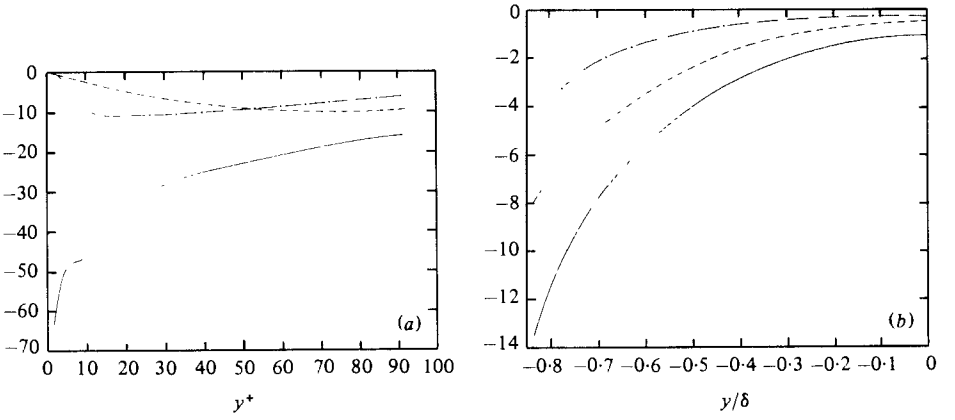


FIGURE 18. Dissipation of turbulent kinetic energy due to molecular and eddy viscosities and the cascade term in the vicinity of the lower wall (*a*) and in the regions away from the wall (*b*):

———, $-(2/Re_\tau)\langle \partial \bar{u}_i''/\partial x_j \, \partial \bar{u}_i''/\partial x_j \rangle$; — — —, $-2\langle \nu_T \, \partial \bar{u}_i''/\partial x_j \, \partial \bar{u}_i''/\partial x_j \rangle$;

—·—, $-2\langle \bar{u}_i'' \, \partial \lambda_{ij}/\partial x_j \rangle$.

were combined. In figure 18, there are separate plots of the dissipation of turbulent kinetic energy due to molecular and eddy viscosity respectively. It can be seen that, near the wall, the dissipation due to eddy viscosity is negligible compared to that due to molecular viscosity. However, in the regions away from the wall, they are comparable. Finally, in figure 18, the cascade term $-\langle \bar{u}_i'' \, \partial \lambda_{ij}/\partial x_j \rangle$ is also plotted. Near the wall, its magnitude is larger than the dissipation due to eddy viscosity, and away from the wall they are of the same order of magnitude. Therefore, as was pointed out in § 2, inclusion of $\langle \bar{u}_i'' \, \partial \lambda_{ij}/\partial x_j \rangle$ in the modelling assumption for the subgrid-scale stresses is not recommended. As long as this term can be evaluated explicitly, one should do so.

## 7. Detailed flow structures

In this section we shall investigate the detailed structure of the computed flow field. This will be done by examining contour plots of instantaneous velocity, pressure, and vorticity field, and by tracking passive particles in the flow. The latter approach is a simulation of laboratory flow-visualization experiments using hydrogen-bubble wire.

Figure 19 shows the contour plot of $\bar{u}''$ in the $(x, z)$-plane at $y^+ = 6{\cdot}26$ and at the non-dimensional time, $t = 4{\cdot}3$. In all the contour plots shown here, positive values are contoured by solid lines and negative values are contoured by dashed lines. In addition, all the instantaneous plots are obtained at the non-dimensional time $t = 4{\cdot}3$. The distinctive feature of the flow patterns in figure 19 is the existence of highly elongated regions of high-speed fluid ($\bar{u}'' > 0$) located adjacent to the low-speed regions. This picture of the flow in the vicinity of the wall is in agreement with laboratory observations. In their visual studies, Runstadler, Kline & Reynolds (1963) and, more recently, other investigators have clearly demonstrated that the viscous sublayer consists of coherent structures of high- and low-speed streaks alternating in the spanwise direction. These studies have also shown that the streaks are the unique characteristic of the wall-layer turbulence, and they are absent in the regions away from the walls. Figure 20 shows the contour plot of $\bar{u}''$ in an $(x, z)$-plane far away from the wall

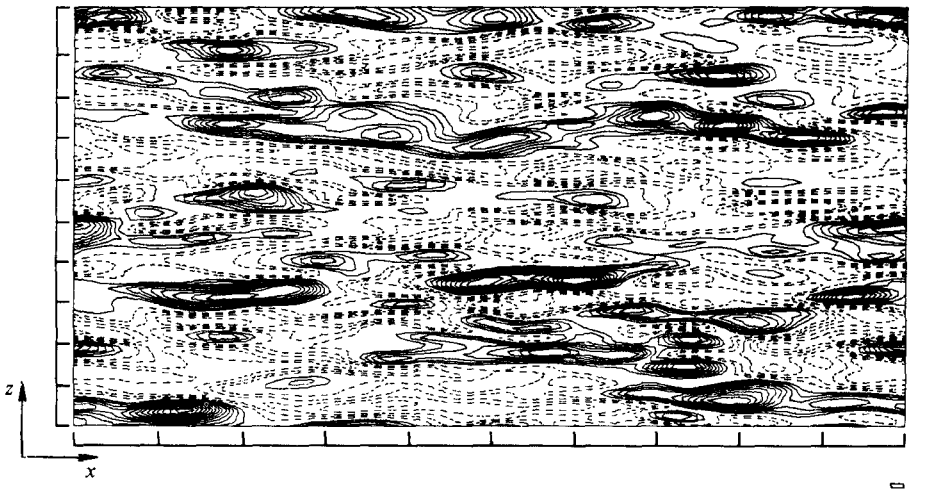


FIGURE 19. Contours of $\bar{u}''$ in the $(x, z)$-plane at $y^+ = 6{\cdot}26$. The rectangle on the lower right-hand corner of the figure represents the computational grid cell in the $(x, z)$-planes. The streamwise extent of the figure is $2\pi\delta(4021\nu/u_\tau)$, and its spanwise extent is $\pi\delta$.

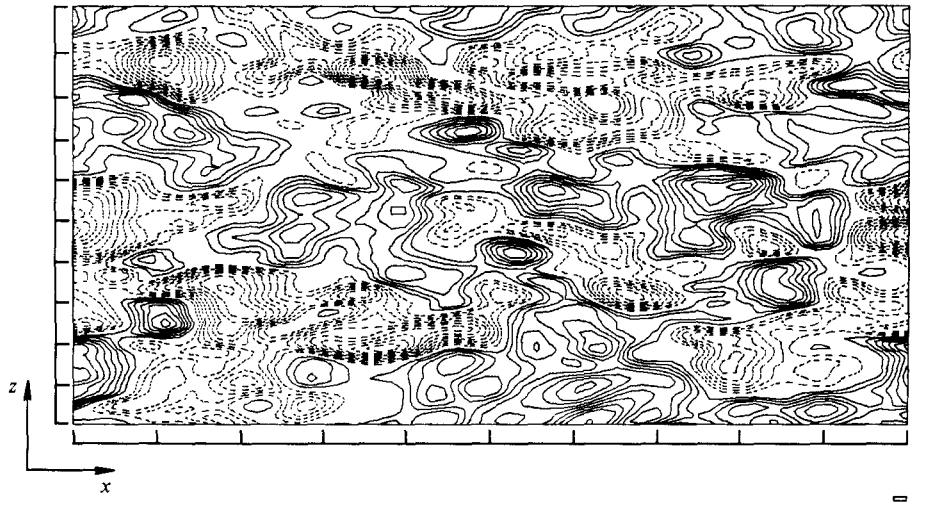


FIGURE 20. Contours of $\bar{u}''$ in the $(x, z)$-plane at $y = -0{\cdot}374$.

($y^+ = 400$). In this region, in agreement with experimental observations, it is clear that the streaks and, for that matter, any definite organized structures are absent in the computed flow patterns.

In figure 19, one can distinguish several localized regions of very high-speed fluid (large concentration of solid lines) that are located on the high-speed streaks. Figure 21 shows the corresponding contour plot of pressure fluctuations, obtained at the same vertical location ($y^+ = 6{\cdot}26$). It can be seen that, in contrast to $\bar{u}''$, the pressure patterns are not elongated in the streamwise direction. However, the regions of high-pressure fluctuations are generally located in the vicinity of the 'pockets' (see Falco 1978) of high-speed fluid. This correspondence together with examination of the contour plots of $\bar{v}$ (see below) suggest that these pockets are 'quasi-stagnation' regions which are formed as a result of the arrival of high-speed fluid to the wall layer. Moreover, the

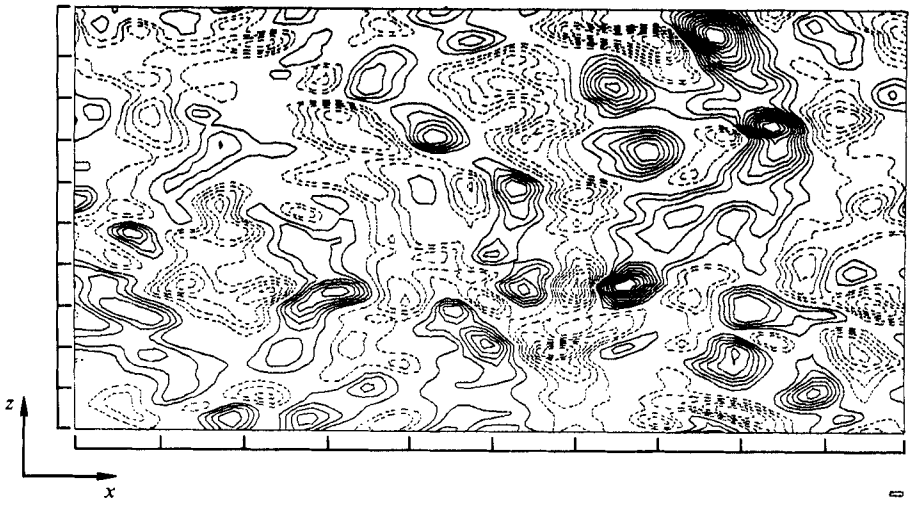


FIGURE 21. Contours of $P$ in the $(x, z)$-plane at $y^+ = 6{\cdot}26$.

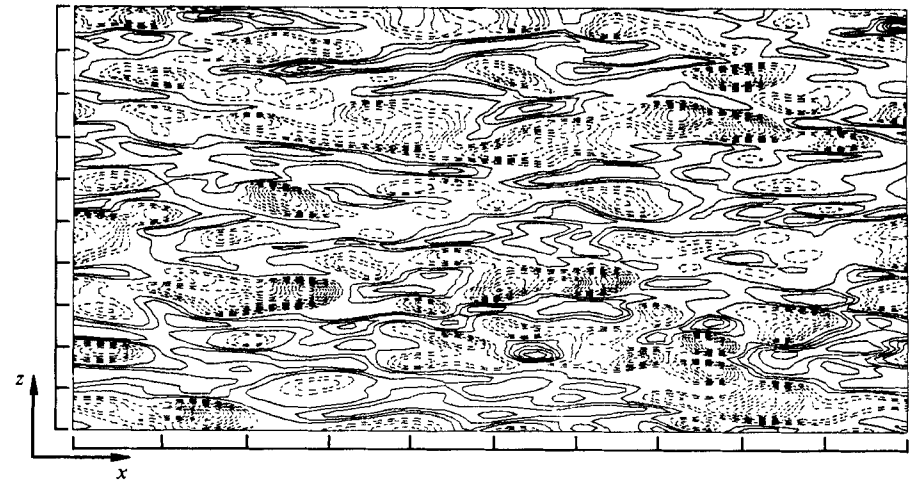


FIGURE 22. Contours of spanwise vorticity fluctuation $\omega_z''$ in the $(x, z)$-plane at $y^+ = 6{\cdot}26$.

contour plots of normal and spanwise velocity fluctuations show that, like the pressure patterns, they do not exhibit elongated streaky structures. These observations imply that the wall layer may be viewed as a bed of low-speed fluid that is constantly subjected to the arrival of energetic eddies from the layers above. These energetic eddies (with the help of the strong mean shear) form the high-speed streaks in the wall region.

Figure 22 shows the contour plot of spanwise vorticity fluctuation,

$$\omega_z'' = \frac{\partial \overline{v}}{\partial x} - \frac{\partial \overline{u}''}{\partial y}$$

in the same $(x, z)$-plane as in figure 19. Virtually all the regions with large vorticity fluctuations are associated with negative $\omega_z''$ (large concentration of dashed lines). In these regions, the streamwise velocity profile has excess momentum with respect to the mean velocity (i.e. $\overline{u}'' > 0$). It should be pointed out that, in the vicinity of the wall,

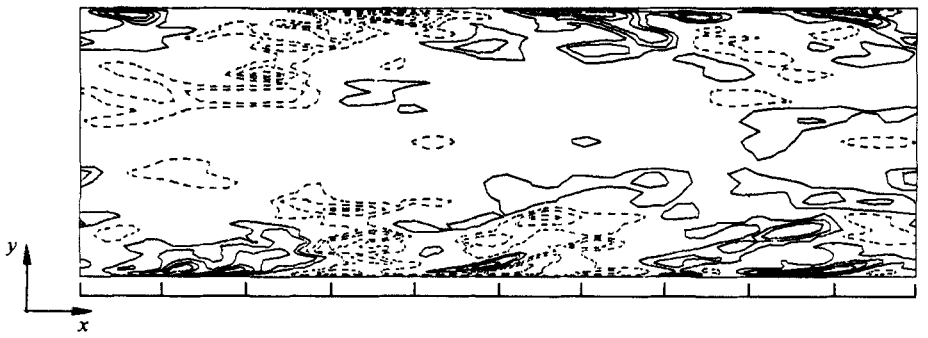


FIGURE 23. Contours of $\overline{u}''$ in the $(x, y)$-plane at $z = 4h_3$. The streamwise extent of the figure is $2\pi\delta(4021\nu/u_\tau)$, and its vertical extent is $2\delta$.


FIGURE 24. Contours of $\overline{v}$ in the $(x, y)$-plane at $z = 4h_3$.

the relatively large positive values of $S(\overline{u}'')$ (figure 8) indicate that the existence of regions with $\overline{u}'' < 0$ are more probable that those with $\overline{u}'' > 0$. However, the structures with large magnitudes of $\overline{u}''$ are most likely associated with positive values of $\overline{u}''$. This is in agreement with the above observations.

Figures 23 and 24 show the $\overline{u}''$ and $\overline{v}$ patterns in an $(x, y)$ plane ($z = 4h_3$) which pass through the high-speed region in the lower left-hand corner of figure 19. In figure 24, a positive $\overline{v}$ (the solid lines) represents fluid moving in the positive $y$-direction, and a negative $\overline{v}$ (the dashed lines) represents fluid moving in the negative $y$-direction. It can be seen that, in the vicinity of the walls, the high-speed fluid elements ($\overline{u}'' \gg 0$) correspond to the sweep event, i.e. $\overline{v} < 0$ near the lower wall, and $\overline{v} > 0$ near the upper wall. On the other hand, the low-speed fluid elements are generally being ejected from the wall regions. Clearly, both the sweep and ejection events have a positive contribution to the production of turbulent kinetic energy. One of the distinct features of figure 23 is that the high-speed structures near the walls are inclined at oblique angles with respect to the walls. This is the consequence of the action of mean shear on any fluid element from the outer layers that is moving toward the walls. Similar large-scale structures have been identified in the laboratory by Rajagopalan & Antonia (1979). In their measurements, they report the mean angle of inclination of these structures to be 13°.

Figures 25 and 26 show the contour plots of $\overline{u}''$ and $\overline{v}$ in a $(y, z)$-plane ($x = 0$). In these plots, only the lower half of the channel is shown. Throughout a significant portion of the region displayed, there is a negative correlation between $\overline{u}''$ and $\overline{v}$. Some of the regions where the correlation between $\overline{u}''$ and $\overline{v}$ is negative extend from the wall region

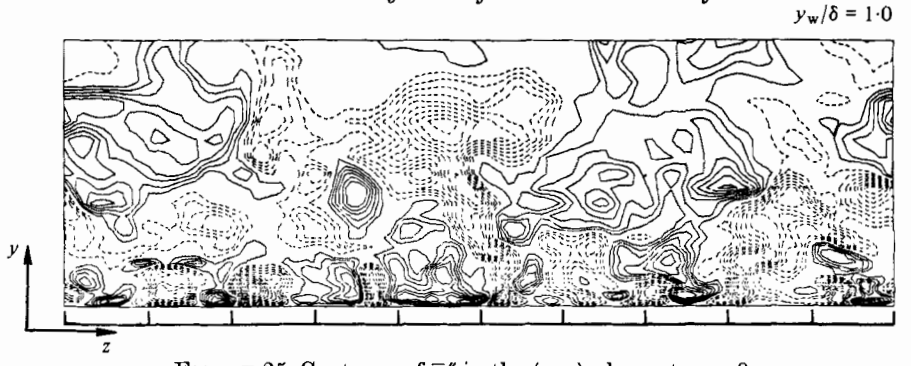


FIGURE 25. Contours of $\overline{u}''$ in the $(y, z)$-plane at $x = 0$.
(Only the lower half of the channel is shown.)

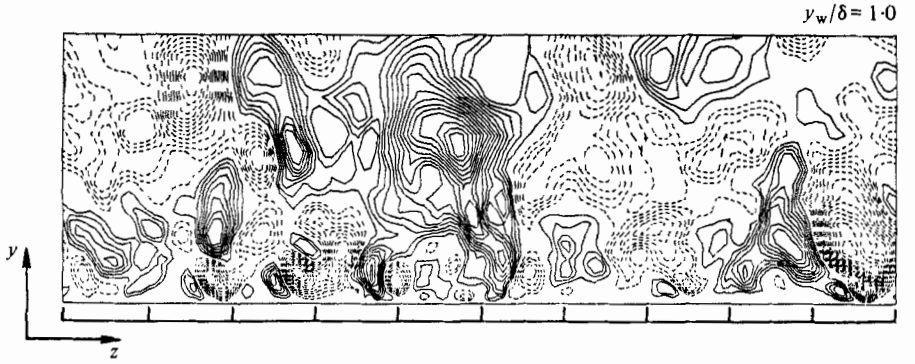


FIGURE 26. Contours of $\overline{v}$ in the $(y, z)$-plane at $x = 0$.
(Only the lower half of the channel is shown.)

to the channel centreline. In the wall region, the vertical and spanwise extent of the eddies is significantly smaller than in the regions away from the wall. In particular, near the wall in figure 24 the array of high- and low-speed fluid is clearly discernible.

Figure 27 shows the $\overline{u}''$, $\overline{v}$, and $\overline{w}$ patterns in the close vicinity of the wall ($y^+ < 46$, $y_w/\delta < 0{\cdot}072$) in the same $(y, z)$-plane as in figures 25 and 26. Here, the region near the wall is magnified, and hence the contour lines are highly distorted. In figure 27 (*a*), the mean spacing between two adjacent high-speed streaks (or low-speed ones) is about 250 in the wall units. The mean streak spacing can also be obtained from the $R_{11}(y_w = 0{\cdot}025, r_3)$ profile in figure 7. In this figure, the negative peak occurs at $r^+ \simeq 125$. This is the distance between two adjacent high- and low-speed streaks. Therefore, the corresponding distance between two high- (or low-) speed streaks is about 250 in the wall units. These two values are, surprisingly, in good agreement with each other but are considerably larger than the generally accepted value of $\lambda_{3m}^+ \simeq 100$. Therefore, as was pointed out in § 3 for the Reynolds number considered in this study, the computational grid resolution is inadequate to resolve the streaks at their proper scale. However, as we have seen, the computed flow patterns, in the wall region, do exhibit the streaky structures at the finest scale permitted by the grid. The $R_{11}(y_w = 0{\cdot}025, r_3)$ profile from case 1 in table 1 shows that the mean streak spacing in that calculation is about 315 in the wall units. Thus, there is a definite improvement in the computed streak spacings with refinement of the computational grid resolution. The effect of

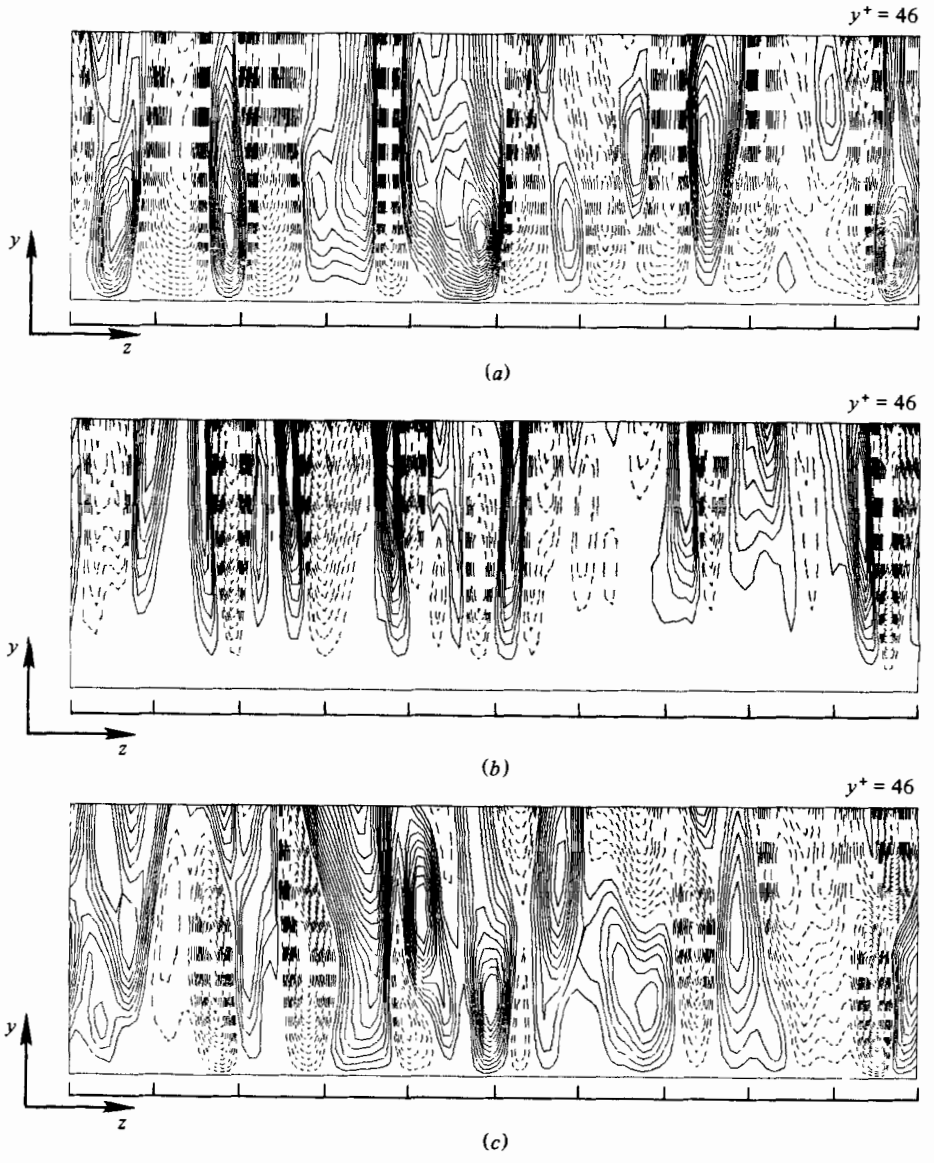


FIGURE 27. Contours of $\overline{u}''$ (*a*), $\overline{v}$ (*b*), and $\overline{w}$ (*c*) in the $(y, z)$-plane ($y^+ < 46$, $y_w/\delta < 0{\cdot}072$) at $x = 0$.

computational grid resolution on other turbulent correlations varies, depending on the variables involved and the order of the statistical correlations. As a general rule, the contribution of the subgrid-scale eddies to lower-order single-point statistical correlations (e.g. $\langle \overline{u}_1 \rangle$, $\langle \overline{u}_i''^2 \rangle$) is negligible (except near the wall), but their contribution to higher and multi-point statistical correlations can be appreciable.

In figure 27(*b*), one can see an array of positive and negative regions of $v$-contour lines that correspond to fluid moving away from and toward the wall. Intense shear layers are located at the interface between the energetic fluid streams moving toward and away from the wall. These shear layers may undergo Helmholtz-type instabilities

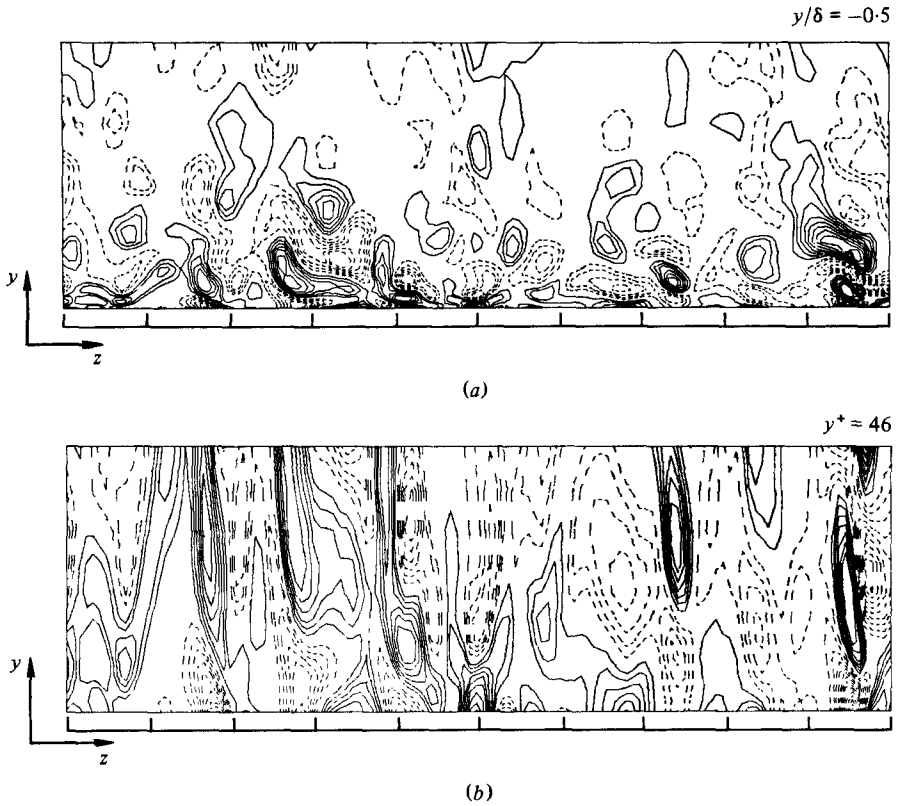


FIGURE 28. Contours of streamwise vorticity fluctuations in the $(y, z)$-plane at $x = 0$; (*a*) $y < -0{\cdot}5$; (*b*) $y^+ < 46$.

in the $(y, z)$-plane that result in the formation of streamwise vortices. These vortices can be clearly identified in figure 28, where the contour plot of $\omega_x$ in the same $(y, z)$-plane is shown.

Comparison of figures 27 (*b*) and (*c*) demonstrate that, in the close vicinity of the wall ($y^+ < 10$), the high-speed vertical streams with negative normal component of velocity produce a flow pattern similar to that of a jet impingement on a plate. On the other hand, the high-speed vertical streams with positive normal component of velocity are formed from two streams with opposite velocities in the spanwise direction. Since the high-speed fluid elements arriving at the wall region are more energetic than the viscous-dominated fluid moving away from the wall, there is a net transfer of energy from the normal component of turbulence intensity to the horizontal components (the splatting effect). This appears to be the reason for the behaviour of the pressure–strain correlations in the vicinity of the wall (figure 11). In addition, it should be noted that the impingement of fluid from outer layers on the wall leads to stretching of spanwise vorticity fluctuations (as well as streamwise vorticity) which can be an important mechanism for its amplification.

Near the wall, in figure 27 (*c*), one can see large gradients of the spanwise velocity component in the normal direction. On the other hand, owing to the wall-suppression effect, the vertical component of turbulence intensity is degraded there. Large values of $\partial w/\partial y$ lead to high values of streamwise vorticity fluctuations in the neighbourhood

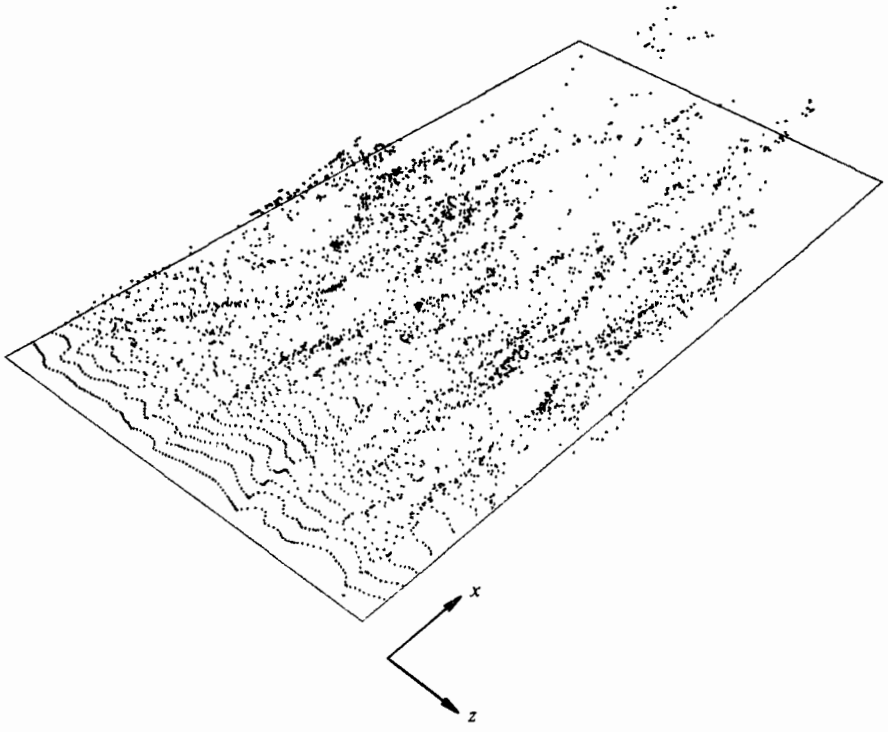


FIGURE 29. Particles generated from a '$z$-wire' located at $y^+ = 12$.

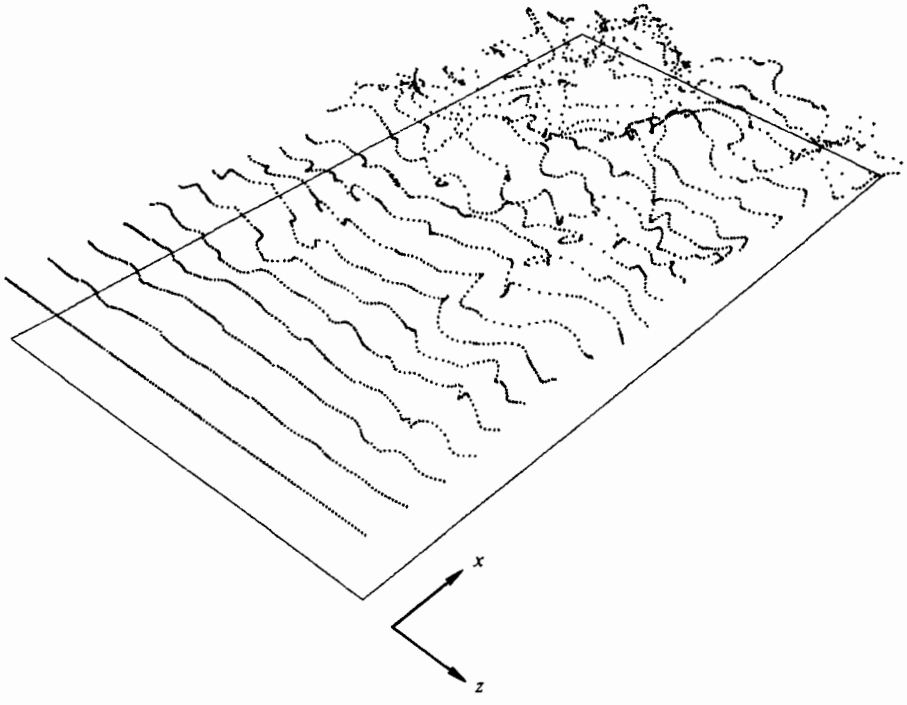


FIGURE 30. Particles generated from a '$z$-wire' located at $y = -0{\cdot}5$.

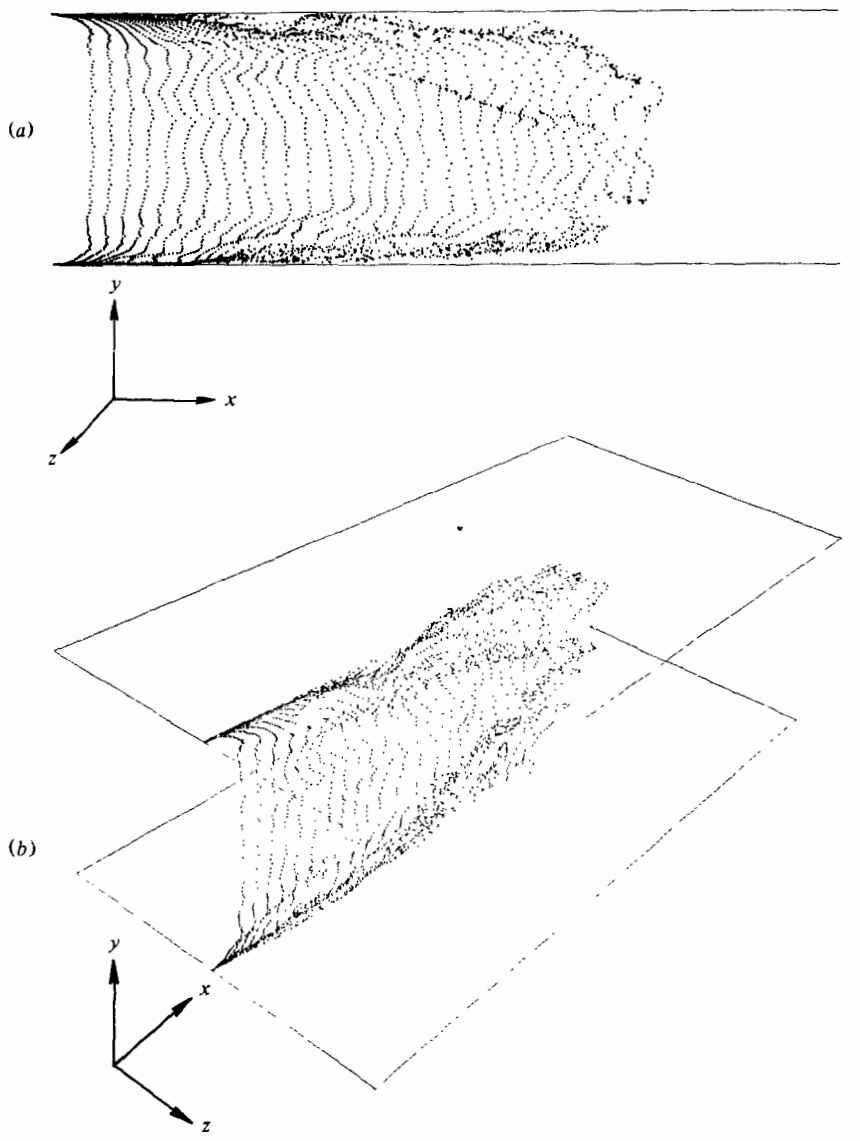


FIGURE 31. Particles generated from a vertical wire extended between the two channel walls: (*a*) two-dimensional view; (*b*) three-dimensional view.

of the wall. In figure 28, it can be seen that the regions with large $\omega_x$ are concentrated near the wall. Here, two distinct areas can be identified: the first is slightly above the wall ($10 < y^+ < 40$), where the large amplitudes of $\omega_x$ are due to revolving fluid elements induced by the intense shear layers shown in figure 27(*b*); the second is in the immediate neighbourhood of the wall ($y^+ < 10$), where the splatting effect and no-slip boundary conditions lead to large values of $\partial w/\partial y$, and consequently $\omega_x$. In figure 9, the profile of $\langle \omega_x^2 \rangle^{\frac{1}{2}}$ attained its maximum at the wall, and displayed a local maximum at $y^+ \simeq 30$. The maximum at the wall is a result of the splatting effect, and the local maximum is located in the first region described above.

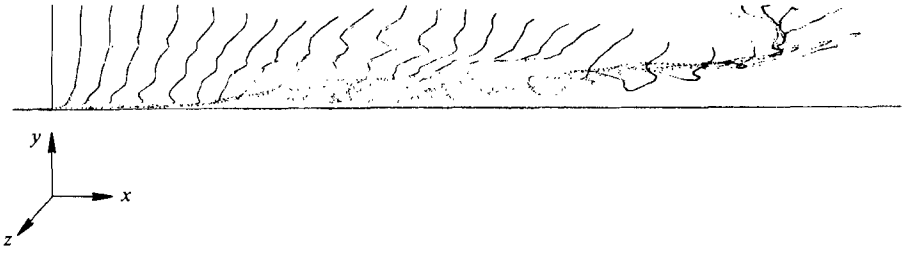


FIGURE 32. Particles generated from a vertical wire extended from the lower wall to $y = -0{\cdot}5$.

So far, we have examined the eddy structure of the turbulent channel flow by considering two-dimensional contour plots of instantaneous velocity, pressure, and vorticity field. To gain a better insight into the unsteady dynamics of the flow, a computer motion picture simulating flow-visualization experiments with hydrogen-bubble wires was made. Several sequences of film were generated. At regular intervals in each sequence ($\Delta T = 0{\cdot}015$ in non-dimensional time units), 128 particles were generated along a line either parallel or normal to the walls. These particles were followed until the memory capacity of the graphic display unit was depleted. Here, we briefly discuss some of the still photographs taken from the film.

Figure 29 shows the particles generated along a line parallel to the $z$-axis ('$z$-wire') and located near the lower wall ($y^+ = 12$). In this figure, the wall-layer streaks are clearly evident. On several occasions when viewing the motion picture, it was observed that the particles generated near the wall were violently ejected to regions as far away from the wall as $y^+ \simeq 400$.

Figure 30 shows the time history of the particles generated along a '$z$-wire' which is located distant from the wall ($y^+ = 319$). It can be seen that the coherent streaky structures that are the characteristic of wall-layer turbulence are absent in the regions away from the walls.

In figure 31, the time history of the particles generated along a line normal to the walls is shown. The formation of inflexional velocity profiles and strong shear layers near the walls is very similar to the corresponding photographs obtained by Kim *et al.* (1971) in their flow-visualization studies. This resemblance is even more pronounced in figure 32, where 128 particles were generated along the same vertical line, as in figure 31, but extended from the lower wall to $y = -0{\cdot}5$. Here, one can see several profiles with multiple inflexion points. In addition, in this figure, the formation of a streamwise vortex with an axis of rotation which is tilted outward in the flow direction and its ultimate breakup are clearly discernible.

## 8. Summary and conclusions

In this study, turbulent plane Poiseuille flow has been simulated numerically at a moderate Reynolds number. Most of the calculations were carried out with 516096 grid points on the ILLIAC IV computer. The agreement of the computed mean-velocity profile and turbulence statistics with experimental data is good.

The resolvable portion of the statistical correlations appearing in the Reynolds-stress equations was calculated. The role and relative importance of the various terms in these equations were discussed.

The structure of the flow field was examined in some detail. It was found that, in agreement with experimental observations, the computed flow pattern in the wall region was characterized by coherent structures of low- and high-speed streaks alternating in the spanwise direction. In this region, the large-amplitude, streamwise velocity fluctuations were due primarily to the arrival of high-speed fluid elements from adjacent layers. The regions with large-amplitude, streamwise vorticity $\omega_x$ were concentrated near the wall. Slightly above the wall, these regions contained revolving fluid elements induced by strong shear layers in the cross-stream plane. In the immediate neighbourhood of the wall, the splatting effect led to large magnitudes of $\omega_x$ and instigated transfer of energy from the normal component of turbulent kinetic energy to the horizontal components.

With three-dimensional, time-dependent, numerical simulation of turbulence, one is capable of obtaining detailed, instantaneous information about the flow at thousands of spatial locations. This information can be used effectively to study the structure and statistical properties of the flow, and their relation to each other. Furthermore, with the aid of computer graphics and the ability to move back in time and recreate an event in the flow after it has already been observed, one has the unique opportunity to study the mechanics of turbulent shear flows. Thus, with the anticipated advances in computer technology, it is expected that in the near future numerical simulation of turbulent flows will make important contributions to turbulence research.

This work was carried out in co-operation with the Thermo- and Gas-Dynamic Division of the Ames Research Center, NASA. We are indebted to our colleagues, A. Leonard, R. S. Rogallo, M. Rubesin and A. A. Wray, Ames Research Center, and D. R. Chapman, J. H. Ferziger and W. C. Reynolds, Stanford University, for numerous helpful discussions during the course of this study.

## REFERENCES

ANTONOPOULOS-DOMIS 1981 Large-eddy simulation of a passive scalar in isotropic turbulence. *J. Fluid Mech.* **104**, 55–79.

BATCHELOR, G. K. 1953 *The Theory of Homogeneous Turbuence.* Cambridge University Press.

BLAKE, W. K. 1970 Turbulent boundary-layer wall-pressure fluctuations on smooth and rough walls. *J. Fluid Mech.* **44**, 637–660.

BRODKEY, R. S., WALLACE, J. M. & ECKELMANN, H. 1974 Some properties of truncated turbulence signals in bounded shear flows. *J. Fluid Mech.* **63**, 209–224.

CHAPMAN, D. R. 1979 Computational aerodynamics development and outlook. *A.I.A.A. J.* **17**, 1293–1313.

CLARK, J. A. 1968 A study of incompressible turbulent boundary layers in channel flow. *Trans. A.S.M.E.* D, *J. Basic Engng* **90**, 455.

CLARK, J. A. & MARKLAND, E. 1970 Vortex structures in turbulent boundary layers. *Aero. J.* **74**, 243–244.

COMTE-BELLOT, G. 1963 Contribution a l'étude de la turbulence de conduite. Doctoral thesis, University of Grenoble.

CORCOS, G. M. 1962 *Univ. Calif., Inst. of Engrg Res. Rep., Series* 183, no. 1.

DALY, J. & HARLOW, F. H. 1970 Transport equations in turbulence. *Phys. Fluids* **13**, 2634–2649.

DEARDORFF, J. W. 1970 A numerical study of three-dimensional turbulent channel flow at large Reynolds numbers. *J. Fluid Mech.* **41**, 453–480.

ELLIOTT, J. A. 1972 Microscale pressure fluctuation measured within the lower atmospheric boundary layer. *J. Fluid Mech.* **53**, 351–383.

EMMERLING, R. 1973 The instantaneous structure of the wall pressure under a turbulent boundary layer flow. *Max-Planck-Inst. für Strömungsforschung Rep.* no. 9/1973.

FALCO, R. E. 1978 The role of outer flow coherent motions in the production of turbulence near a wall. In *Coherent Structures of Turbulent Boundary Layers* (ed. C. R. Smith & D. E. Abbott). A.F.O.S.R./Lehigh.

GRÖTZBACH, G. & SCHUMANN, U. 1979 Direct numerical simulation of turbulent velocity-, pressure-, and temperature-fields in channel flows. In *Turbulent Shear Flows I* (ed. F. Durst, B. E. Launder & F. W. Schmidt), pp. 379–385. Springer.

HARLOW, F. H. & WELCH, J. E. 1965 Numerical calculation of time-dependent viscous incompressible flow. *Phys. Fluids* **8**, 2182.

HINZE, J. O. 1975 *Turbulence*, 2nd edn. McGraw-Hill.

HUSSAIN, A. K. M. F. & REYNOLDS, W. C. 1975 Measurements in fully developed turbulent channel flow. *Trans. A.S.M.E.* I, *J. Fluids Engng* **97**, 568–578.

KIM, H. T., KLINE, S. J. & REYNOLDS, W. C. 1971 The production of turbulence near a smooth wall in a turbulent boundary layer. *J. Fluid Mech.* **50**, 133.

KIM, J. & MOIN, P. 1979 Large eddy simulation of turbulent channel flow–ILLIAC IV calculation. In *Turbulent Boundary Layers–Experiments, Theory, and Modeling, The Hague, Netherlands. AGARD Conf. Proc.* no. 271.

KLINE, S. J., REYNOLDS, W. C., SCHRAUB, F. A. & RUNSTADLER, P. W. 1967 The structure of turbulent boundary layers. *J. Fluid Mech.* **30**, 741–773.

KREPLIN, H. & ECKELMANN, M. 1979 Behavior of the three fluctuating velocity components in the wall region of a turbulent channel flow. *Phys. Fluids* **22**, 1233–1239.

KWAK, D., REYNOLDS, W. C. & FERZIGER, J. H. 1975 Three-dimensional time-dependent computation of turbulent flows. *Dept Mech. Engng, Stanford Univ., Rep.* TF–5.

LAUFER, J. 1954 The structure of turbulence in fully developed pipe flow. *NACA Rep.* no. 1174.

LEONARD, A. 1974 On the energy cascade in large-eddy simulations of turbulent fluid flows. *Adv. Geophys.* **18**A, 237–248.

MANSOUR, N. N., MOIN, P., REYNOLDS, W. C. & FERZIGER, J. H. 1979 Improved methods for large eddy simulation of turbulence. In *Turbulent Shear Flows I* (ed. F. Durst, B. E. Launder & F. W. Schmidt), pp. 379–385. Springer.

MOIN, P. & KIM, J. 1980 On the numerical solution of time-dependent, viscous, incompressible fluid flows involving solid boundaries. *J. Comp. Phys.*, **35**, 381–392.

MOIN, P., REYNOLDS, W. C. & FERZIGER, J. H. 1978 Large eddy simulation of incompressible turbulent channel flow. *Dept Mech. Engng, Stanford Univ., Rep.* TF–12.

ORSZAG, S. A. 1972 Comparison of pseudospectral and spectral approximation. *Stud. Appl. Math.* **51**, 253–259.

RAJAGOPALAN, S. & ANTONIA, R. A. 1979 Some properties of the large structure in a fully developed turbulent duct flow. *Phys. Fluids* **22**, 614–622.

RUNSTADLER, P. W., KLINE, S. J. & REYNOLDS, W. C. 1963 An investigation of the flow structure of the turbulent boundary layer. *Dept Mech. Engng, Stanford Univ., Rep.* MD–8.

SABOT, J. & COMTE-BELLOT, G. 1976 Intermittency of coherent structures in the core region of fully developed turbulent pipe flow. *J. Fluid Mech.* **74**, 1976, 767–796.

SCHUMANN, U. 1973 Ein Verfahren zur direckten numerischen Simulation turbulenter Strömungen in Platten- und Ringspaltkanälen und über seine Anwendung zur Untersuchung von Turbulenzmodellen. Dissertation, Fac. Engng TH Karlsruhe, KFK 1854.

SCHUMANN, U. 1975 Subgrid scale model for finite difference simulations of turbulent flows in plane channels and annuli. *J. Comp. Phys.* **18**, 376–404.

SCHUMANN, U., GRÖTZBACH, G. & KLEISER, L. 1980 Direct numerical simulation of turbulence. In *Prediction Methods for Turbulent Shear Flows* (ed. W. Kollmann), pp. 123–258. Hemisphere.

SHAANAN, S., FERZIGER, J. H. & REYNOLDS, W. C. 1975 Numerical simulation of turbulence in the presence of shear. *Dept Mech. Engng, Stanford Univ., Rep.* TF–6.

TOWNSEND, A. A. 1956 *The Structure of Turbulent Shear Flow.* Cambridge University Press.

VAN DRIEST, E. R. 1956 On turbulent flow near a wall. *J. Aero. Sci.* **23**, 1007–1011.

WILLMARTH, W. W. 1965 Corrigendum to Willmarth & Wooldridge (1962). *J. Fluid Mech.* **21**, 107–109.

WILLMARTH, W. W. 1975 Pressure fluctuations beneath turbulent boundary layers. *Ann. Rev. Fluid Mech.* **7**, 13–38.

WILLMARTH, W. W. & WOOLDRIDGE, C. E. 1962 Measurement of the fluctuating pressure at the wall beneath a thick turbulent boundary layer. *J. Fluid Mech.* **14**, 187–210.